MusE GAs FLOw and Wind (MEGAFLOW) II. A study of gas accretion around z ≈ 1 star-forming galaxies with background quasars

Johannes Zabl, Nicolas F. Bouché, Ilane Schroetter, Martin Wendt, Hayley Finley, Joop Schaye, Simon Conseil, Thierry Contini, Raffaella A. Marino, Peter Mitchell, et al.

MNRAS **000**, 1–23 (2018) Preprint 30 July 2019 Compiled using MNRAS LATEX style file v3.0

MusE GAs FLOw and Wind (MEGAFLOW) II. A study of gas accretion around $z \approx 1$ star-forming galaxies with background quasars ⋆

Johannes Zabl,[1,2]† Nicolas F. Bouché,[1,2] Ilane Schroetter,[3,1] Martin Wendt,[4,5] Hayley Finley,[6,1] Joop Schaye,[7] Simon Conseil,[2] Thierry Contini,[1] Raffaella A. Marino,[8] Peter Mitchell,[2] Sowgat Muzahid,[7] Gabriele Pezzulli,[8] Lutz Wisotzki[5]

[1] *Institut de Recherche en Astrophysique et Planétologie (IRAP), Université de Toulouse, CNRS, UPS, F-31400 Toulouse, France*
[2] *Univ Lyon, Univ Lyon1, Ens de Lyon, CNRS, Centre de Recherche Astrophysique de Lyon UMR5574, F-69230 Saint-Genis-Laval, France*
[3] *GEPI, Observatoire de Paris, CNRS-UMR8111, PSL Research University, Univ. Paris Diderot, 5 place Jules Janssen, 92195 Meudon, France*
[4] *Institut für Physik und Astronomie, Universität Potsdam, Karl-Liebknecht-Str. 24/25, 14476 Golm, Germany*
[5] *Leibniz-Institut für Astrophysik Potsdam (AIP), An der Sternwarte 16, 14482 Potsdam, Germany*
[6] *Stockholm University, Department of Astronomy and Oskar Klein Centre for Cosmoparticle Physics, AlbaNova, University Centre SE-10691, Stockholm, Sweden*
[7] *Leiden Observatory, Leiden University, PO Box 9513, NL-2300 RA Leiden, the Netherlands*
[8] *Department of Physics, ETH Zürich,Wolfgang-Pauli-Strasse 27, 8093 Zürich, Switzerland*

Accepted XXX. Received YYY; in original form ZZZ

ABSTRACT

We use the MusE GAs FLOw and Wind (MEGAFLOW) survey to study the kinematics of extended disk-like structures of cold gas around $z \approx 1$ star-forming galaxies. The combination of VLT/MUSE and VLT/UVES observations allows us to connect the kinematics of the gas measured through Mg II quasar absorption spectroscopy to the kinematics and orientation of the associated galaxies constrained through integral field spectroscopy. Confirming previous results, we find that the galaxy-absorber pairs of the MEGAFLOW survey follow a strong bimodal distribution, consistent with a picture of Mg II absorption being predominantly present in outflow cones and extended disk-like structures. This allows us to select a *bona-fide* sample of galaxy-absorber pairs probing these disks for impact parameters of 10–70 kpc. We test the hypothesis that the disk-like gas is co-rotating with the galaxy disks, and find that for 7 out of 9 pairs the absorption velocity shares the sign of the disk velocity, disfavouring random orbits. We further show that the data are roughly consistent with inflow velocities and angular momenta predicted by simulations, and that the corresponding mass accretion rates are sufficient to balance the star formation rates.

Key words: galaxies: evolution – galaxies: formation – galaxies: kinematics and dynamics – galaxies: haloes – (galaxies:) quasars: absorption lines

1 INTRODUCTION

A number of arguments (theoretical and observational) indicate that galaxies cannot be closed boxes with an *ab-initio* fixed reservoir of gas. Indeed, numerical simulations show that galaxies grow from the accretion of cool intergalactic gas (via the cosmic web), a process most efficient in galaxies with luminosities lower than L^* (White & Frenk 1991; Birnboim & Dekel 2003; Kereš et al. 2005; Dekel & Birnboim 2006; Dekel et al. 2009; van de Voort et al. 2011; L'Huillier et al. 2012) owing to the short cooling times in these halos (Rees & Ostriker 1977; Silk 1977). Observationally, a number of indirect arguments support the notion that galaxies need to continuously replenish their gas, implying that they are continuously fed by the accretion of gas from the intergalactic medium (IGM), as reviewed in Fox & Davé (2017).

Originally, the most common indirect argument comes from the G-dwarf problem (van den Bergh 1962; Schmidt

⋆ Based on observations made with ESO Telescopes at the La Silla Paranal Observatory under programme IDs 094.A-0211, 095.A-0365, 096.A-0609, 096.A-0164, 097.A-0138, 097.A-0144, 098.A-0216, 098.A-0310, 099.A-0059, 293.A-5038
† E-mail: johannes.zabl@univ-lyon1.fr

1963), which says that the metallicity distribution of G stars in the solar neighbourhood is not consistent with the closed-box expectations, and the data can be reconciled with chemical models provided that there is a significant amount of metal poor infall (Larson 1972a,b; Lynden-Bell 1975; Pagel & Patchett 1975; Casuso & Beckman 2004). Another common indirect argument relies on the observed short gas depletion time-scales ($\equiv M_{\rm gas}/{\rm SFR}$), seen in local and distant galaxies to be typically 0.5–2 Gyr (e.g. Daddi et al. 2010; Freundlich et al. 2013; Genzel et al. 2015; Tacconi et al. 2010, 2013, 2018; Scoville et al. 2016, 2017; Schinnerer et al. 2016; Saintonge et al. 2013, 2016, 2017). These short depletion times imply that the observed amount of gas available is too low to sustain their star formation rate (SFR) for more than a few Gyr, i.e. it is not enough to support the galaxies' future star formation. A third indirect argument comes from the slow decline of the cosmic HI density as a function of redshift (e.g. Péroux et al. 2003; Neeleman et al. 2016) tied to the gas content of galaxies (Wong & Blitz 2002).

As mentioned, in low mass galaxies hosted by halos below the virial shock mass threshold ($M_h \lesssim 10^{11-12} M_\odot$) gas accretion is expected to be very efficient (e.g. White & Frenk 1991; Birnboim & Dekel 2003; Kereš et al. 2005; Faucher-Giguère et al. 2011; Nelson et al. 2015; Correa et al. 2018). Once inside the galaxy dark matter halo, the accreted gas is expected to orbit the galaxy, bringing along not just fuel for star formation but also angular momentum (e.g. Stewart et al. 2011b, 2013, 2017; Danovich et al. 2015). In this context, the accreting material coming from the large-scale filamentary structure should form a warped, extended gaseous structure (e.g. Pichon et al. 2011; Kimm et al. 2011; Shen et al. 2013; Danovich et al. 2015; Stewart et al. 2017), which co-rotates with the central disk and is sometimes referred to as a 'cold-flow disk' (Stewart et al. 2011b, 2013, 2017).

This 'cold-flow disk' scenario leads to large gaseous ($T \sim 10^4$ K) structures, which could in part become the large disks often seen around galaxies in HI 21cm surveys and extending 2–3 times beyond the stellar radius (e.g. Bosma 1981; Putman et al. 2009; Bigiel et al. 2010; Kreckel et al. 2011; Wang et al. 2016; Ianjamasimanana et al. 2018).

At higher redshifts, the 'cold-flow disk' scenario is expected to lead to distinct signatures in absorption systems with $N_{\rm HI}$ of 10^{17} to 10^{21} cm^{-2} seen in background quasar sight-lines (Dekel et al. 2009; Kimm et al. 2011; Fumagalli et al. 2011; Stewart et al. 2011a, 2013; Goerdt et al. 2012; van de Voort & Schaye 2012). In particular, some of the infalling gas kinematics is expected to be offset from the galaxy's systemic velocity when observed in absorption along the sight-lines of background quasars (Stewart et al. 2011a), because the gas is partly rotationally supported.

These expected signatures are testable against observations with suitably located background sources such as quasars (Barcons et al. 1995; Steidel et al. 2002; Chen et al. 2005; Kacprzak et al. 2010, 2011; Bouché et al. 2013; Turner et al. 2014; Bouché et al. 2016; Ho et al. 2017; Rahmani et al. 2018), bright galaxies (Diamond-Stanic et al. 2016), or directly in redshifted absorption lines in galaxy spectra (*down-the-barrel*; Coil et al. 2011; Rubin et al. 2012; Martin et al. 2012; for review see Rubin 2017).

Among background sources, background galaxies are more numerous, but their usefulness is usually limited by the typically low S/N unless one reverts to a stacking approach as in Bordoloi et al. (2011). By contrast, background quasars are rarer, but allow one to obtain more informations, such as the gas location from the host, gas ionization properties (e.g. Muzahid et al. 2015; Lehner et al. 2016; Prochaska et al. 2017) and most importantly the gas kinematics (e.g. Barcons et al. 1995; Steidel et al. 2002; Kacprzak et al. 2010; Bouché et al. 2013, 2016; Ho et al. 2017). Among those, Ho et al. (2017) demonstrated the existence of co-rotating structures at $z \approx 0.2$ in a sample of half-dozen galaxies, a step forward from the individual analyses of Bouché et al. (2013) and Bouché et al. (2016)

Progress in sample size has been slow in spite of decades of research with galaxy-quasar pairs, as studies investigating the connections between the host galaxy kinematics and the low-ionization absorption line kinematics were limited to $\sim$ 50 pairs (see Kacprzak 2017, for a recent review). Less than half of these have orientations favourable to study extended gas disks (accretion cases) (Barcons et al. 1995; Steidel et al. 2002; Chen et al. 2005; Kacprzak et al. 2010, 2011; Bouché et al. 2013, 2016; Ho et al. 2017; Rahmani et al. 2018).

Thanks to the MUSE (Multi Unit Spectroscopic Explorer; Bacon et al. 2006, 2010) instrument on the VLT (Very Large Telescope) with its unprecedented field-of-view (1'×1') and sensitivity, the situation is about to change significantly by taking advantage of the combination of MUSE kinematics and high-resolution UVES (Ultraviolet and Visual Echelle Spectrograph; Dekker et al. 2000) data. Indeed, we recently started the MuseE GAs FLOw and Wind (MEGAFLOW) survey (Bouché et al. in prep), which consists of MUSE+UVES observations of 22 quasar fields, each with multiple (three or more) strong (> 0.5–0.8Å) MgII absorbers at redshifts $0.3 < z_{\rm abs} < 1.5$ selected from the JHU-SDSS catalog (Zhu & Ménard 2013). The MEGAFLOW survey leads to one of the largest surveys of MgII absorber-galaxy pairs with spectroscopic and kinematic information, with about 80+ galaxy-quasar pairs suitable to study either outflows (as in Schroetter et al. 2016, hereafter Paper I) or accretion (as in Bouché et al. 2016, this work) depending on the apparent location of the quasar with respect to the galaxy major-axis.

In this paper, we present results on nine galaxy-quasar pairs suitable for characterising the kinematics of accreting gas, while the wind cases will be presented in a companion paper (Schroetter et al. in prep). After briefly introducing the MEGAFLOW survey (§2), we discuss in §3 the observation and reduction strategy both for the MUSE and UVES data. The selection of the nine galaxy-quasar pairs of this study from the $\approx$ 80 absorbers pairs in the MEGAFLOW survey is discussed in §4. Then, we infer kinematical and physical properties of the selected galaxies and their host halos in §5. As the main result of our work, we compare galaxy to absorber kinematics in §6, with a focus on testing for co-rotation and potential radial infall.

Throughout this paper, we use the ΛCDM standard cosmological parameters: $H_0 = 70$ km s^{-1}, $\Omega_\Lambda = 0.7$, and $\Omega_{\rm m} = 0.3$. All distances are proper. Further, we assume a Chabrier (2003) stellar Initial Mass Function (IMF) and all stated magnitudes are on the AB system (Oke 1974). When we refer in the following to [OII] without additional wavelength qualifier, we refer to the [OII]$\lambda\lambda$3727, 3729 doublet. The prefix 'pseudo' in pseudo-filter and pseudo-spectrum refers to the fact that these were created from the MUSE

data cube. All stated uncertainties are 68% confidence intervals. The nine galaxy-absorber pairs can be identified throughout by uniquely assigned colours.

2 THE MEGAFLOW SURVEY

2.1 Motivation

Since the initial work of Bergeron (1988); Bergeron & Boissé (1991) and Steidel (1995); Steidel et al. (2002), there is a well established association between the cool (T $\sim 10^4$ K) component of the CGM traced by the low-ionization Mg II doublet seen in absorption in background quasar spectra and star-forming galaxies. Large samples of galaxy-quasar pairs are rare and difficult to construct owing to the difficulty in finding the host galaxy responsible for the Mg II absorption, which is often a painstaking process requiring deep imaging (preferably from the *Hubble Space Telescope* (HST)) and multi-object spectroscopy, with the added problems of the quasar point spread function (PSF) blocking the view directly along the line-of-sight. One of the largest samples of Mg II selected galaxy-quasar pairs with morphological data is the MAGIICAT sample (Churchill et al. 2013; Nielsen et al. 2013a,b, 2015, 2016), which consists of 123 isolated foreground galaxies with associated Mg II detections at $0.07 \leq z \leq 1.1$.

Surveys of galaxy-quasar pairs such as the MAGIICAT sample suffer from two major limitations, namely that they must rely on photometric pre-selection (i.e. suffer from redshift incompleteness) and that they lack kinematical information on the host galaxies. Both of these limitations must be overcome using expensive follow-up spectroscopic campaigns. This can be partially by-passed with integral field unit (IFU) surveys as described in Bouché (2017) because IFU surveys can simultaneously (i) locate the host galaxy; (ii) determine the host photometric and kinematics properties; (iii) determine the host morphological properties in most cases; and (iv) allow for proper PSF subtraction in case of small impact parameters.

2.2 The survey

With the field-of-view ($1' \times 1'$), sensitivity, and wavelength coverage of the VLT/MUSE instrument ($\sim$ 4800 Å–9300 Å), building large samples of absorber-galaxy pairs is now feasible with only a handful of observing nights. In particular, we started the MEGAFLOW survey of 22 quasar fields, which aims at building a sample of $\sim$ 100 galaxy-quasar pairs. In order to reach this goal, we selected quasars from the JHU-SDSS Mg II absorber catalogue (Zhu & Ménard 2013) which had at least three (or more) Mg II absorbers within the redshift range from 0.4 to 1.5, suitable for [O II] based identification of star-forming galaxies in the MUSE wavelength range.[1] In addition, we imposed that the rest-frame equivalent width of Mg II λ2796, $EW_0^{\lambda 2796}$, of the three required absorbers be greater than 0.5Å, with a preference given to sight-lines with multiple $EW_0^{\lambda 2796} > 0.8$Å absorbers. The restriction on Mg II rest equivalent width $EW_0^{\lambda 2796} > 0.5$Å was chosen because the host galaxy is then expected to be within ≈100 kpc of the quasar line-of-sight, i.e. matching the field-of-view of MUSE, given the well known anti-correlation between the impact parameter and $EW_0^{\lambda 2796}$ (Lanzetta & Bowen 1990; Bergeron & Boissé 1991; Steidel 1995; Bordoloi et al. 2011; Chen et al. 2010; Nielsen et al. 2013a; Werk et al. 2013). A slightly less stringent equivalent width threshold of $EW_0^{\lambda 2796} > 0.3$Å is often used in the literature to separate strong Mg II absorbers from weak Mg II absorbers (e.g. Churchill et al. 1999). Our 22 quasar sight-lines serendipitously include several (10) absorbers with 0.3Å $< EW_0^{\lambda 2796} <$ 0.5Å in the right redshift range. We included these absorbers in the analysis. Even so their equivalent widths are slightly below our survey threshold, the galaxy-absorber association for absorbers of this strength is still expected to be sufficiently robust. In total, the 22 quasar sight-lines contain 79 strong Mg II absorbers with $EW_0^{\lambda 2796} > 0.3$Å with $0.51 < z < 1.45$.

3 DATA

Each quasar field was observed with MUSE and each quasar was followed up with the high-resolution spectrograph UVES at the VLT.

3.1 MUSE observations

We observed all 22 quasar fields with the VLT/MUSE instrument over the period September 2014 to May 2017[2] as part of guaranteed time observations (GTO). A full description of the data for all 22 fields will be given in a future paper describing the full survey (Bouché et al., in prep.). Briefly, all except three fields were observed for at least 2hr, i.e. the resulting exposure times are $\geq$ 6 ks. Observation details are listed in Table 1.

3.1.1 Data reduction

We reduced the data using the ESO MUSE pipeline version v1.6 (Weilbacher et al. 2012, 2014, 2016). First, each individual exposure was processed by the *scibasic* recipe to produce a table (hereafter called pixtable) containing relative locations, wavelength, counts, and an estimate of the variance. This recipe removes the instrumental signatures by applying daily calibrations (lamp flat-fields, bias, twilight-flat illumination corrections) and calibrates the wavelength scale (based on daily arc-lamps). Further, *scibasic* also applies the geometric solution (determined once per GTO run) for each of the 24 IFUs. Bad pixels corresponding to known CCD defects (columns or pixels) are also masked at this time. For each exposure we also used an 'illumination' exposure, which are short flats, to correct for flux variations on the slices due to small temperature changes between the daily calibration exposures and the science exposures.

[1] [O II] can be observed with MUSE starting from $z \approx 0.3$, but the JHU-SDSS Mg II catalog does not include absorbers below z=0.4.

[2] This was the period of data used for our first full analysis of the data, which is the basis for this paper and a companion paper discussing outflows (Schroetter et al. in prep). Observations were completed in November 2018.

Second, the individual pixtables were flux-calibrated (using the response from daily standards), telluric corrected (using a telluric absorption estimate from the flux-standard), sky-subtracted, astrometrically calibrated, and resampled onto a cube (using the drizzle algorithm) with the pipeline's *scipost* recipe. However, clear variations of the residual background level between individual slices were visible in white-light images created from the cube, caused by imperfections from the flat-fielding/illumination correction. To mitigate these imperfections we used a self-calibration strategy, as in Bacon et al. (2015, 2017), which is conceptually similar to the *CubeFix* method developed by Cantalupo (in prep., see also Borisova et al. 2016 and Marino et al. 2018). Essentially, it consists of normalizing the background in all slices to the overall background level.

In practice [3], we were using the 'selfcalibrate' method in the python package *MPDAF* (MUSE Python Data Analysis Framework) v2.3dev [4] (Piqueras et al. 2017). This method computes the multiplicative corrections necessary to bring each slice to the reference background level, which is determined by the mean sky background across the field. Consequently, it requires as input a 'positioned'[5] pixtable with the sky subtraction turned off, and an object mask. We used *SExtractor* on the white light images (as described above) to produce the object masks and we reran the scipost from the 24 scibasic pixtables to produce a 'positioned' scipost pixtable per exposure. In this rerun of scipost, sky subtraction and correction for barycentric velocity were switched off. Because the self-calibration does successfully remove the slice-to-slice variations but fails to remove the sharp flat-field imperfections visible at the edges of the IFUs, we simply masked the affected regions in the *scibasic* pixtables used as input.

After performing the self-calibration, we resampled the corrected positioned pixtables to datacubes using again the *scipost* recipe. Here, we performed the sky subtraction, barycentric correction, and use the same 3D output world coordinate system (WCS) grid for each of the cubes. We then used the software-package *Zurich Atmosphere Purge* (*ZAP*) (Soto et al. 2016a,b) to remove skyline residuals from each datacube, which makes use of a principal component analysis PCA analysis [6] using *cftype='fit'* and using an improved object mask created from the white-light pseudo-images. After manual inspection of the individual cubes and masking of visible satellites tracks, we combined the cubes. For those fields where the seeing between individual exposures was strongly differing, we weighted each exposure with the inverse of the full width at half maximum (FWHM) of the PSF.

[3] Starting with version v2.4 of the MUSE DRS, which was not available at the time when we reduced the data for this work, the self-calibration is directly implemented. The steps described in this paragraph would no longer be necessary when using DRS v2.4 or later.
[4] Available at https://git-cral.univ-lyon1.fr/MUSE/mpdaf.
[5] A '*pixtable_positioned*' is a pixtable where the spatial position information for each pixel is given in absolute R.A. and Dec.
[6] Available at https://github.com/musevlt/zap.

3.1.2 Data characterization

In order to assess the image quality, we measured the PSF on the quasar itself in the combined cubes by fitting an elliptical 2D Moffat profile (Moffat 1969). Due to the large wavelength range covered by the MUSE data (from 4800 to 9300 Å), we measured the PSF as a function of wavelength using 100 Å wide pseudo-filter images at five different wavelengths separated by 1000 Å, and interpolated these measurements for other wavelengths. We first performed the PSF measurement on each of these images using a Moffat profile with β set to 2.5. The Moffat FWHM values at 7050 Å range from 0″.53 to 0″.98 across the 22 fields, with a median value of 0″.76. Second, we also determined the wavelength dependence of the PSF with the *Pampelmuse* code (Kamann et al. 2013) using a Moffat profile with the β parameter free. Overall, the difference between the fixed-β values and the free-β *Pampelmuse* values are different by a median of 5% and at most 14%.

In order to obtain a realistic estimate for our sensitivity to [O II] emitters, we estimated the 5σ point source detection limit in a pseudo-NB filter with an appropriate width of 400 km s^{-1}. A filter width of 400 km s^{-1} gives the optimal S/N for the [O II] $\lambda\lambda$3727, 3729 doublet when assuming a line-width of FWHM $\approx$ 50 km s^{-1}. In the spatial direction, we assumed a circular detection aperture with radius of 1.5×FWHM$_{\rm Moffat}$. This aperture size gives the optimal S/N for a point source convolved with a Moffat PSF with $\beta = 2.5$ in the background limited case. By using an estimate for the per-pixel noise and scaling it to the number of pixels spanned by the assumed spatial size and filter width, we derived an estimate for the total noise within the aperture. Subsequently, we multiplied this noise estimate by 1/0.52 in order to correct for aperture losses both in the spatial and the wavelength directions.

The wavelength dependent per-pixel noise was estimated from the pipeline's variance map of a cube in source free regions. Using this estimate we derive a typical 5σ [O II] detection limit $\sim 4 \times 10^{-18} \times (FWHM_{\rm Moffat}/0''.6) \times (T_{\rm exp}/6ks)^{-0.5}$ erg s^{-1} cm^{-2} in MUSE's most sensitive wavelength region around 7000 Å, which corresponds to a [O II] redshift of $z \approx 0.9$. This derived [O II] flux limit corresponds to an unobscured SFR limit of 0.07 M$_\odot$ yr^{-1} (cf. Eq. (2)). The line flux sensitivity both short-wards and long-wards of this wavelength decreases somewhat, with the ends of the relevant wavelength range having about a factor 1.5 lower sensitivity. The SFR sensitivity further changes according to the change of the luminosity distance with redshift. The above estimates assume sky-line free regions. While this means that the sensitivity can in practice be lower, [O II] is a doublet with a separation larger than the spectral resolution of MUSE and hence usually a substantial part of the doublet is in sky-line free regions. Finally, the presence of the background quasar can impact the [O II] detection limit, if a galaxy happens to be right in front of the quasar. Our quasars have r-band magnitudes between 19.5 and 17.5, with a median of 18.5. The detection limit would increase to $\sim 11 \times 10^{-18}$ erg s^{-1} cm^{-2} for a galaxy exactly in front of a 18.5 mag quasar, assuming the same seeing and exposure time as above. In addition, there might remain systematic residuals after the quasar light was subtracted, which are difficult to generalise. However, as the wavelength range

covered by the [O II] doublet is small, neither the PSF nor the quasar continuum change much over the relevant wavelength range. Therefore, a continuum subtraction with two well chosen off-band filters typically leaves very small quasar residuals.

3.2 UVES observations

3.2.1 Observations

Each quasar was also observed with the VLT high-resolution spectrograph UVES with settings chosen in order to cover Mg II $\lambda\lambda$2796, 2803, Mg I λ2852, Fe II λ2600, and when possible other elements such as Ti, Zn. We used a slit width of 1″.0, resulting in a spectral resolution of R≈38000 ($FWHM \approx 8$km s^{-1}). Further, we chose a 2x2 readout binning for all observations. The UVES observations are presented in Table 2.

3.2.2 Data reduction

The Common Pipeline Language (CPL version 6.3) of the UVES pipeline was used to bias correct and flat-field the exposures and then to extract the wavelength and flux calibrated spectra. After the standard reduction, the custom software UVES POst PipeLine Echelle Reduction (POPLER) (Murphy 2016) version 0.66 was used. The processing of the spectra, including the air-to-vacuum correction, was carried out with this software. The spectra of echelle orders were re-dispersed and combined onto a common vacuum heliocentric wavelength scale and a pixel width of 1.3 km s^{-1}. Left-over cosmic rays were removed by σ-clipping. The automatic procedure of cosmic ray clipping was verified by visual inspection and the continuum was fitted with fourth order Chebyshev polynomials and adjusted manually whenever deemed necessary.

4 SAMPLE

As motivated in §2, MEGAFLOW is a Mg II absorber-selected survey and as such the first step is to identify the galaxies whose CGM is associated with the selected strong Mg II absorption. In this section, we describe how we carefully identify all galaxies within the MUSE field-of-view (FoV) down to the deepest limits (in §4.1), a critical step since Mg II absorbers could be associated with multiple galaxies. In §4.2, we describe how we assign a primary galaxy to the Mg II absorbers. In §4.3, we describe the sub-sample of galaxy-absorber pairs suitable for this paper, whose focus is on the extended gaseous disks around star-forming galaxies.

4.1 Galaxy detections

Our main identification strategy is based on narrowband (NB) images constructed at the redshift of each absorber. Aside from a visual inspection of [O II] NB images using QFitsView [7], we performed an automatic source detection designed to detect the lowest SNR galaxies (from both emission lines and absorption lines).

The automatic detection algorithm is based on 'optimized' multi-NB images. The 'optimized' means that we weighted at each spaxel the pixels in the wavelength direction with the squared S/N of the respective pixels. This efficiently filters out sky-lines and gives most weight to wavelengths where the source signal is strong. The 'multi-NB' means that the pseudo-NB filter has transmittance not only around a single emission line but at multiple lines simultaneously with the individual passbands matched in velocity width. Each of the passbands was continuum subtracted by using the median flux density in two off-band NB filters to the blue and red, respectively.

The multi NB images are created by combining NB-images for multiple emission lines (each over the same velocity range). This included [O II] and depending on the redshift Hβ and/or [O III]λ5007. Each NB image is created with a width of [8] 400 km s^{-1}. For comparison, a virial velocity of 400 km s^{-1} corresponds to a virial mass of $\sim 10^{13} M_{\odot}$, which is the typical halo mass for a galaxy with stellar mass, M_* of $10^{11} M_{\odot}$. For each absorber redshift, we created three NB pseudo-images at three different velocity offsets from the absorber redshifts, namely at -250, 0, 250 km s^{-1}. We then performed source detection with *SExtractor* (Bertin & Arnouts 1996) on each of these three images, centred at -250, 0, 250 km s^{-1}. We optimize *SExtractor* to detect low SNR objects in order to reduce the possibility of missing real candidates, but this leads to a number of false positives, which have to be removed manually.

We also searched for quiescent galaxies specifically, by creating an 'optimized' multi NB filter including both lines of the Ca H&K doublet. Quiescent galaxies at the right redshift have negative fluxes in the continuum-subtracted NB filter. Therefore, we ran *SExtractor* in this case on inverted images. Again, we checked for all candidates that the signal is indeed coming from Ca H&K, hence confirming them to be at the right redshift.

In summary, our algorithm is able to detect both emission line galaxies and galaxies with mere H&K absorption.

4.2 Mg II host association

With its 60″ wide FoV, MUSE covers at redshift $z = 1$ about 480kpc, so $\sim$ 240kpc in each direction from the quasar. To put this into perspective, the virial radius of a $z = 1$ galaxy with M^* and its corresponding halo mass of $\log(M_{\rm h}/{\rm M}_{\odot}) \approx 12.4$ is $\approx$ 200kpc. Consequently, the MUSE observations allow us to identify the galaxies associated with the absorption, even if the associated absorption would be all the way out at the virial radius. However, due to the anti-correlation between impact parameter and $EW_0^{\lambda 2796}$ (Lanzetta & Bowen 1990; Chen et al. 2010; Nielsen et al. 2013a), we expect most of the strong Mg II absorbers to originate from gas at impact parameters, b, smaller than the virial radius. This justifies to focus in the Mg II host association on galaxy-absorber pairs which have $b \lesssim 100$ kpc.

From our MEGAFLOW survey of 79 Mg II absorbers

[7] Available at http://www.mpe.mpg.de/~ott/QFitsView/.

[8] The width of the [O II] NB filters was extended by the width of the separation of the [O II] doublet.

MUSE Observations								
Quasar	R.A.	Dec.	T_{exp}	Seeing (G.)	Seeing (M.)	Date-Obs	Prog. IDs	Refs
(1)	(2)	(3)	(4)	(5)	(6)	(7)	(8)	(9)
J0145p1056	01:45:13.1	+10:56:27	6.0	1.03	0.85	2015-11-12, 2016-08-29	096.A-0164(A), 097.A-0138(A)	This work

Table 1. Details of MUSE observations for the 22 MEGAFLOW quasar fields as used in this study. **The full table with all 22 fields is in Table C1 of the Supplementary Appendix.** (1) Quasar/Field identifier; (2) Right ascension of the QSO [hh:mm:ss; J2000]; (3) Declination of the QSO [dd:mm:ss; J2000]; (4) Total MUSE exposure time [ks]; (5) Seeing FWHM measured at 7050Å by fitting a Gaussian [arcsec]; (6) Seeing FWHM measured at 7050Å by fitting a Moffat profile with $\beta = 2.5$ [arcsec]; (7) Date of Observations; (8) ESO Program IDs; (9) Reference.

UVES Observations									
Quasar	R.A.	Dec.	z_{em}	T_{exp}	Seeing	Date-Obs	Setting	Prog. IDs	Refs
(1)	(2)	(3)	(4)	(5)	(6)	(7)	(8)	(9)	(10)
J0145p1056	01:45:13.1	+10:56:27	0.94	12020	0.6	2015-11-11, 2016-09-03, 2016-10-28	390 & 564	096.A-0609, 097.A-0144, 098.A-0310	This work

Table 2. Details of UVES observations for the 22 MEGAFLOW Quasars. **The full table with all 22 quasars is in Table C2 of the Supplementary Appendix.** (1) Quasar identifier; (2) Right ascension of QSO [hh:mm:ss; J2000]; (3) Declination of QSO [dd:mm:ss; J2000]; (4) Emission redshift of the QSO; (5) Total UVES exposure time split into settings [s]; (6) Seeing FWHM measured by DIMM split into settings [arcsec] ; (7) Date of Observations; (8) UVES settings (Central wavelengths of gratings in [nm]); (9) ESO Program IDs;

with $EW_0^{\lambda 2796} \gtrsim 0.3$ Å, we detect one or more galaxies in 75% (59/79) of the cases within 100 kpc. When there is at least one galaxy, we find that 41 (10) absorbers have one (two) galaxies within 100 kpc, respectively, accounting together for the majority (51/59) of the sample. We choose the absorbers with a maximum of two galaxies within 100 kpc, in order to study isolated galaxies, and avoid groups where a unique host association becomes not practicable. However, when there are two galaxies within 100 kpc, a decision needs to be made whether one of the two galaxies should be identified with the absorption. We decide that this is the case if the galaxy with the smaller impact parameter has also the higher [O II] flux (4 out of the 10). This decision is motivated by the anti-correlations of $EW_0^{\lambda 2796}$with b and the correlation with SFR ($\propto$ [O II] luminosity, see §5.3) (Lan & Mo 2018). This results in a final sample of 45 galaxy-absorber associations, which we refer to in the following as 'primary' associations.

While one potential caveat with this quasar-galaxy pair identification is that it depends on the depth of the data (down to $f_{[O\,II]} \gtrsim 4 \times 10^{-18}$ erg s^{-1} cm^{-2}), the final sub-sample used for this study (in §4.3) will happen to have $f_{[O\,II]} > 4 \times 10^{-17}$ erg s^{-1} cm^{-2}, implying that the satellite missed by our selection ought to be ≈ 10 times fainter than these primary galaxies.

4.3 Geometrical classification and sub-sample selection

Since the main goal of our present work is to study kinematics of the approximately co-planar, possibly co-rotating and accreting gas, we selected galaxy-absorber pairs with orientations where the quasar sight-line is most favourable for intersecting the presumed extended gaseous disk (e.g. Stewart et al. 2017) and is the least favourable to galactic winds. This can be ensured using the azimuthal angle α (as in Bordoloi et al. 2011; Bouché et al. 2012; Kacprzak et al. 2012; Schroetter et al. 2015; Ho et al. 2017), since outflows are expelling baryons from the galaxy in the direction of least resistance/density, i.e. more or less perpendicularly to the star-forming disk. The azimuthal angle α is the angle between the apparent quasar location and the galaxy major axis, as indicated in Fig. 1.

Determining α does require a robust measurement of the galaxies' position angles, and to a lesser extent inclinations, i, in order to remove face-on galaxies where α is undefined. The position angles were determined by fitting the morphological and kinematic parameters jointly from the [O II] doublet using the *GalPak*^{3D} (Bouché et al. 2015) algorithm (see §5.1). We also checked the morphological parameters obtained directly from the continuum 2D flux maps with *GALFIT* (See section A of the Supplementary Appendix).

Fig. 2 shows the distribution of the primary galaxies in the $\alpha - i$ plane, where the top panel shows the α histogram, demonstrating a strong bimodal distribution of strong Mg II absorption around galaxies. Therefore, strong Mg II absorption is preferably found either along the minor-axis or the major-axis of 45 primary galaxies, which confirms the earlier results of Bouché et al. (2012) and Kacprzak et al. (2012). In addition, one should note that this non-random distribution arises without making any pre-selection on the orientation of the galaxies and also supports our primary galaxy identification (§4.2) because the α's would be randomly distributed if our primary galaxies were unrelated to the absorption.

From this result, the galaxy-quasar pairs used in this paper are selected with the following criteria:

(i) A primary galaxy identification was possible (see sec. 4.2), i.e. we excluded cases where the identification with a single galaxy is ambiguous or not possible;

(ii) The primary galaxy has an [O II] flux $> 3 \times 10^{-17}$ erg s^{-1} cm^{-2}, i.e. we did not include galaxies that are too faint to obtain robust kinematics (and position angles (PA) & inclinations) at the depth of the data;

(iii) The orientation is favourable for extended gaseous disks, i.e. the azimuthal angle is $|\alpha| < 40^\circ$ and the inclination is $i > 40^\circ$ (see Fig. 2);

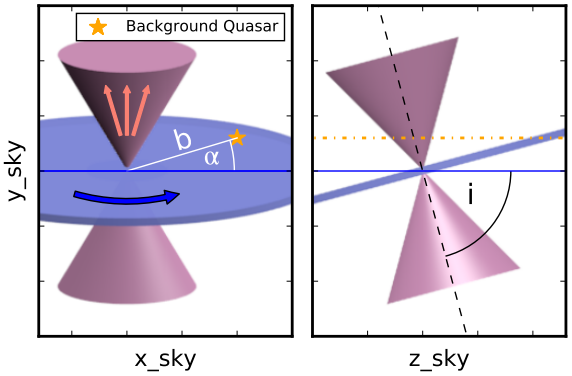

Figure 1. Assumed geometry of the cold CGM. **Left:** CGM geometry as observed on the sky-plane, where $x_{\rm sky}$ is without loss of generality aligned with the disk's projected major axis. The impact parameter b and the azimuthal angle α are the polar coordinates of the background quasar (orange) on the sky-plane. **Right**: Same geometry as seen from the side, where $z_{\rm sky}$ is along the line-of-sight. i is the inclination of the disk on the sky.

(iv) The primary galaxy is not a clear merger and does not have strong AGN signatures.

After applying (i) we are left with 45 galaxy-absorber pairs. Removing faint galaxies with $f_{[\rm O\,II]} \lesssim 3 \times 10^{-17}$ erg s^{-1} cm^{-2} with criteria (ii), leaves 33 galaxies. Applying the main geometric selection (iii) leaves a sample of 10 galaxies. With one galaxy [9] excluded by criterion (iv) results in a final sample of nine galaxy-absorber pairs, which are listed in Table 3. Two of the selected primary galaxy-absorber pairs have a second galaxy within 100 kpc. Incidentally, all of the selected primary galaxies happen to have $f_{[\rm O\,II]} > 4 \times 10^{-17}$ erg s^{-1} cm^{-2}.

The 9 galaxies selected for this accretion study are indicated in the $\alpha - i$ plot (Fig. 2) as thick green circles. In this figure, the points are colour-coded according to the [O II] flux. Similarly, Fig. 3 shows the distribution of the accretion sample galaxies compared to all MEGAFLOW primary galaxies in the $\alpha - b$ plane, showing that the we probe a range of impact parameters (b) from a few to 100 *kpc*.

As for none of the quasar sight-lines more than one absorber ended up in the final sample of the present study, we choose to refer in the following for brevity to the absorber simply by a shortened field ID, e.g. *J0103* stands for the absorber at $z = 0.788$ in the field J0103p1332.

4.4 Discussion of individual cases

In Figure 4, and Figs. B1 – B8 of the Supplementary Appendix, we show the entire MUSE FoV for the [O II] NB image centred on the absorber redshift. The images show all galaxies including primary and secondary galaxies, that we identified to be associated with the relevant absorbers and

[9] This galaxy shows clear AGN signatures, e.g. a strong [Ne v]$\lambda\lambda$3346, 3426 detection (Mignoli et al. 2013). While this doublet is not detected in any of the nine remaining galaxies, we cannot rule out AGN contribution with certainty for the sample based on the available data.

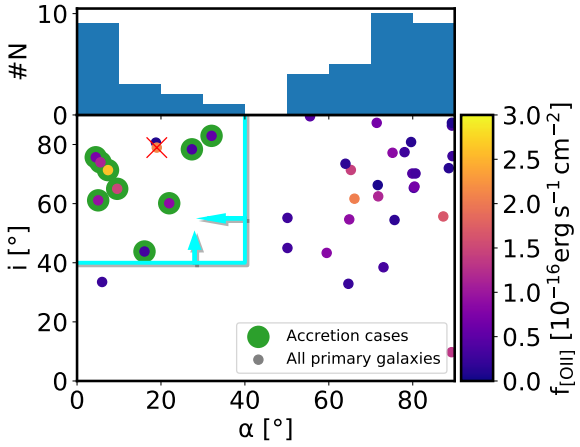

Figure 2. Distribution of the MEGAFLOW primary Mg II host galaxies (see §4.2). In the upper part the α histogram is shown for the points in the $\alpha - i$ plane below. The colour-scale indicates the [O II] flux of the galaxies. The nine points circled in green within the cyan boundaries are suitable (as in §4.3) candidates for this study. One galaxy in the selection region is excluded as it is an AGN (red cross). Two of the 45 primary galaxies are omitted in the α histogram, as we could not obtain robust α for those. Four further primary galaxies are not included in the lower panel, as we could not obtain robust inclinations.

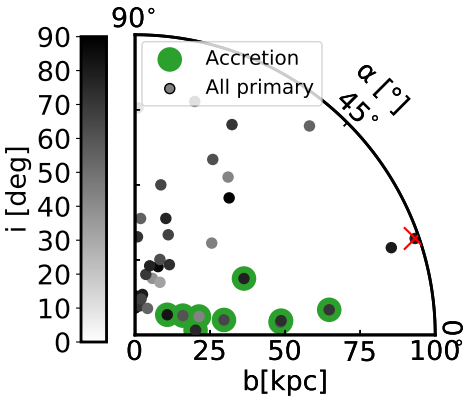

Figure 3. Same galaxies as in Fig. 2, but here shown in the impact parameter vs α diagram. The grey-scale indicates here the inclination. The two objects at $b \approx 50$kpc are overlapping. For an explanation of the red cross see Fig. 2.

are listed in Table 3. The NB images are made from red, green and blue channels, where each channel is a slightly different but overlapping NB image. The green channel is a NB filter of $\pm$150km s^{-1} around the absorber redshift. The blue (red) channel is made at $-(+)$300km s^{-1} from the absorber redshift using a transmittance of 100% and decreases linearly to 0% at $(+) -$ 150km s^{-1}, respectively (a method motivated by Hayashi et al. 2014; Zabl et al. 2016). Hence, the colour represents the velocity offset of the galaxy with respect to the absorber, where blue and red colours represent the corresponding velocity shifts. For galaxies with strong velocity gradients, also the velocity field of individual galaxies is directly visible.

These colour NB images in Figure 4, and Figs. B1 – B8

(see also Table 3) show that for five out of the nine absorbers there is exactly one galaxy associated with the respective absorber over the entire MUSE FoV. For three absorbers (in the fields of *J1039*, *J1358*, and *J2152*), there are two galaxies in the FoV, and for one field, *J0800*, we identified five galaxies in the FoV.

Among the absorbers with two host galaxy candidates, for one of them, *J2152*, the second galaxy is at an impact parameter of 190 kpc, four times further away from the quasar sight-line than the primary galaxy, and is also fainter. For *J1039*, the second galaxy is at $b = 72$ kpc, which is a factor 1.5× further away from the quasar than the primary galaxy. Moreover, this second galaxy is aligned so that a potential outflow cone would be covered by the quasar sight-line ($\alpha = 68°$) and is part of the wind analysis of Schroetter et al. (in prep.). This situation needs to be kept in mind for the discussion of the absorption profiles (see §5.5). In the third field with two galaxies, *J1358*, the second galaxy is only at slightly larger impact parameter than the primary galaxy ($b = 32$ kpc vs $b = 40$ kpc). However, the second galaxy has only about 10% of the primary galaxy's [O II] flux.

For *J0800* we identified five galaxies in the FoV, but only one of them is within 100 kpc ($b = 64$ kpc) and the second closest galaxy is a quiescent galaxy that is a factor two further away and at a large velocity offset of $\approx 400\,\mathrm{km\ s^{-1}}$ from the absorber.[10] For this absorber, we will assume that all absorption is associated with the primary galaxy.

5 GALAXY PHYSICAL PROPERTIES

The MUSE data allows us to determine both photometric and kinematic properties for each detected galaxy. In the following, we discuss the physical properties for our sample of nine primary galaxies. In §5.1, we describe how we determined the galaxy kinematics and redshifts. In §5.2, we explain our continuum photometric measurements used for stellar mass estimates. In §5.3, we discuss our SFR estimates based on [O II] fluxes. In §5.4, we derive the halo mass properties. Finally, we describe the absorption properties in §5.5.

5.1 Galaxy kinematics and redshifts

The main ingredient for our study is a robust comparison between galaxy and absorber kinematics. Recent 3D fitting codes (e.g. Bouché et al. 2015; Di Teodoro & Fraternali 2015) allow one to take advantage of the full 3D information provided by IFU data taking into account the spatial PSF and the spectral line spread function (LSF). Here, we measured both the redshift and galaxy kinematics with the 3D algorithm *GalPak*^{3D} (Bouché et al. 2015) and compared the latter to the traditional 2D method using the *CAMEL*[11] code of Epinat et al. (2012).

5.1.1 *Morpho-kinematical modelling*

In order to apply the 3D line fitting tool *GalPak*^{3D} to the [O II] data, we subtracted the continuum by taking the median in each spaxel over a wavelength window of $\pm 1250\,\mathrm{km\ s^{-1}}$ around the centre of the [O II] doublet and excluding the central $\pm 250\,\mathrm{km\ s^{-1}}$.

In short, *GalPak*^{3D} creates a mock [O II] observation [12] from the parametrised 3D model of a disk galaxy, compares it to the data, and finds the posterior of the parameters through Markov chain Monte Carlo (MCMC) sampling. In such a parametrised approach, a choice for rotation curve and light distribution needs to be made. For the rotation curve, we assume throughout an arctan function, $v(R) = v_{\mathrm{max}} \frac{2}{\pi} \arctan(R/r_{\mathrm{turn}})$, where the two free parameters are the maximum velocity v_{max} and the turn-over radius, r_{turn}. For the distribution of the light emitted in [O II], we assumed an exponential disk, $I(R) \propto \exp(-1.68(R/r_{\mathrm{half}}))$.

For compact galaxies, defined as those which have half-light radii smaller than 0.75 times the Moffat's PSF FWHM, we often tested a Gaussian surface-brightness profile (Sercic index $n = 0.5$) and chose the appropriate Sersic profile based on the lowest χ^2. For these compact galaxies, we either limited the allowed range of the turnover radius r_{turn} (to $< 0.8\,r_{\mathrm{half}}$) or fixed the turnover radius to $1/2.7\,r_{\mathrm{half}}$ in order to break potential degeneracies. This value of 2.7 is motivated by the tight relation between rotation curve scale length and disk scale length found in local galaxies by Amorisco & Bertin (2010)[13].

An additional free parameter in our morpho-kinematical model is a radially constant velocity dispersion, σ_0, which is meant to describe a turbulence component added in quadrature to the disk model, i.e. σ_0 is not the total velocity dispersion (see Bouché et al. 2015, for details). All inferred parameters for all nine galaxies are listed in Table 4.

As a consistency check, we created 2D velocity maps from our fitted model, which can be compared to a map created from a more classical pixel-by-pixel velocity fit. The latter we performed with the code *CAMEL*. This code directly fits the [O II] doublet in each pixel. To increase the S/N, we convolved the cube in the spatial direction with a kernel of FWHM=2 pixels. Both the *GalPak*^{3D} and *CAMEL* based velocity maps are shown in Fig. 4 and Figs. B1 to B8 of the Supplementary Appendix. Reassuringly, no strong discrepancies are visible.

5.1.2 *Redshifts*

Our analysis relies heavily on comparing the kinematics of the host galaxy to that of the absorption in the quasar line-of-sight. Thus, this comparison will depend critically on the accuracy of the systemic redshift of the galaxy. While the *GalPak*^{3D} measurements described in §5.1.1 also provided the redshift of the galaxy (see Table 4), we carefully tested the robustness of the *GalPak*^{3D} based redshift through comparison to redshifts inferred using two other methods.

The first of these two comparison methods makes use

[10] Redshift of the quiescent galaxy was determined with *pPXF* (Cappellari & Emsellem 2004; Cappellari 2017).
[11] Available at `https://bitbucket.org/bepinat/camel.git`.

[12] We use a fixed line ratio of 0.8:1.0 per default, except when the observed [O II] doublet ratio deviates strongly from 0.8.
[13] We converted the Amorisco & Bertin (2010) relation between the exponential disk scale-length and the radius where the rotation curve reaches 2/3 of v_{max} to a r_{half} and r_{turn} ratio for an arctan rotation curve.

Fiekd and absorber	Galaxy ID	Coordinate	b	Δv	$f_{[\mathrm{O\,II}]}$	Note
	(1)	(2)	(3)	(4)	(5)	
Field: J0103p1332 $z_{\mathrm{abs}} = 0.788$	**gal_0788_3_25**	01:03:32.37 +13:32:36.1	20	61	7.2 ± 0.1	
Field: J0145p1056 $z_{\mathrm{abs}} = 0.554$	**gal_0554_3_52**	01:45:13.28 +10:56:28.8	22	-97	3.2 ± 0.1	
Field: J0800p1849 $z_{\mathrm{abs}} = 0.608$	**gal_0608_10_108**	08:00:05.20 +18:49:32.6	65	-12	26.0 ± 1.0	a
	gal_608_19_140	08:00:05.41 +18:49:20.5	129	-419	–	b
	gal_608_23_163	08:00:05.03 +18:49:13.1	155	-278	1.06 ± 0.04	
	gal_608_27_322	08:00:03.37 +18:49:56.6	184	-60	0.5 ± 0.1	
	gal_608_30_144	08:00:05.79 +18:49:10.9	201	6	0.7 ± 0.1	
Field: J1039p0714 $z_{\mathrm{abs}} = 0.949$	**gal_0949_6_324**	10:39:36.42 +07:14:32.4	49	141	9.5 ± 0.1	
	gal_0949_9_344	10:39:36.48 +07:14:36.1	72	111	3.1 ± 0.1	c
Field: J1107p1021 $z_{\mathrm{abs}} = 1.048$	**gal_1048_5_359**	11:07:42.71 +10:21:31.4	41	-45	3.8 ± 0.1	
Field: J1236p0725 $z_{\mathrm{abs}} = 0.912$	**gal_0912_2_246**	12:36:24.25 +07:25:50.8	17	34	8.7 ± 0.6	
Field: J1358p1145 $z_{\mathrm{abs}} = 1.418$	**gal_1418_3_291**	13:58:09.26 +11:45:59.2	30	-60	14.8 ± 0.1	d
	gal_1418_5_238	13:58:09.22 +11:45:55.1	40	-186	1.4 ± 0.1	
Field: J1509p1506 $z_{\mathrm{abs}} = 1.046$	**gal_1046_2_351**	15:09:00.10 +15:06:36.5	13	68	5.4 ± 0.2	
Field: J2152p0625 $z_{\mathrm{abs}} = 1.053$	**gal_1053_6_57**	21:52:00.36 +06:25:19.7	49	-68	11.4 ± 0.3	
	gal_1053_23_341	21:51:59.54 +06:25:38.4	187	6	5.7 ± 0.2	

Table 3. Absorber-galaxy identification. Primary galaxies are indicated in bold. (1) ID. The first number in the ID indicates the absorber redshift, the second the impact parameter in arcsec, and the third the position angle between quasar and galaxy in degrees. (2) Right ascension and Declination of galaxy (hh:mm:ss dd:mm:ss; J2000); (3) Impact parameter [kpc]; (4) Velocity offset between absorber redshift, z_{abs}, and redshift of galaxy, z_{gal} [km s^{-1}]; (5) [O II] flux in units of 10^{-17} erg s^{-1} cm^{-2} as obtained from the 1D line flux (fluxes are measured in large *SExtractor MAG_AUTO* apertures, but not aperture corrected).

Note. a) blend w. foreground galaxy; b) passive HK; c) aligned with minor axis to quasar; d) At this redshift Ca H&K falls outside of the MUSE wavelength range and our automatic detection would miss quiescent galaxies without any residual [O II] line emission. As an alternative, we checked here for stellar Mg II λ2796, 2803 absorption, but did not find any additional candidates.

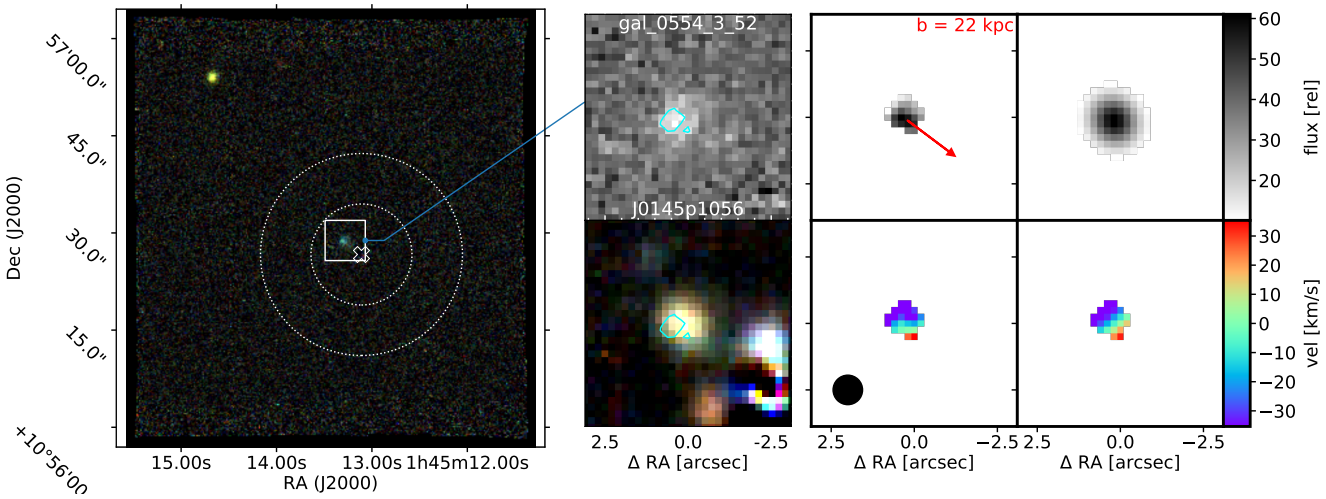

Figure 4. Column 1 (left): Shown is an [O II] NB image covering ±300km s^{-1} around the redshift of the absorber *J0145p1056_0554*. More precisely, three slightly different [O II] NB images were used for each of the three channels of an RGB image. In such an image, emission lines blue-shifted with respect to the absorber redshift appear bluer, while those redshifted will appear redder. The position of the quasar is indicated as a white cross and circles indicate impact parameters corresponding to 50 kpc and 100 kpc. A white box indicates an emission line galaxy associated with the absorber, meaning that the [O II] emission is in the filter. In the shown example there is only the primary galaxy. The remaining NB excess sources are either due to other emission lines than [O II] in the NB filter, which means that they are at other redshifts, or residuals from bright objects. **Column 2:** Top: Simple NB image of the primary galaxy optimised for redshift and width of the [O II] emission. Overlaid is a contour of this image. Below a colour image is displayed, where pseudo V, R, I broadband images constitute blue, green, and red channels, respectively. The same contour as in the NB image is overlaid. **Column 3:** Flux (top) and line-of-sight velocity (bottom) maps obtained from direct fitting with *CAMEL* to the [O II] cube. More details are given in the text. The filled black circle in the lower left corner indicates the FWHM of the Moffat PSF at the observed wavelength of [O II]. **Column 4:** Similar as in column 3, but here the best-fit model flux and velocity maps as obtained from fitting with *GalPak*^{3D} are shown. The zero velocity in the velocity maps is taken from the *GalPak*^{3D} redshift.

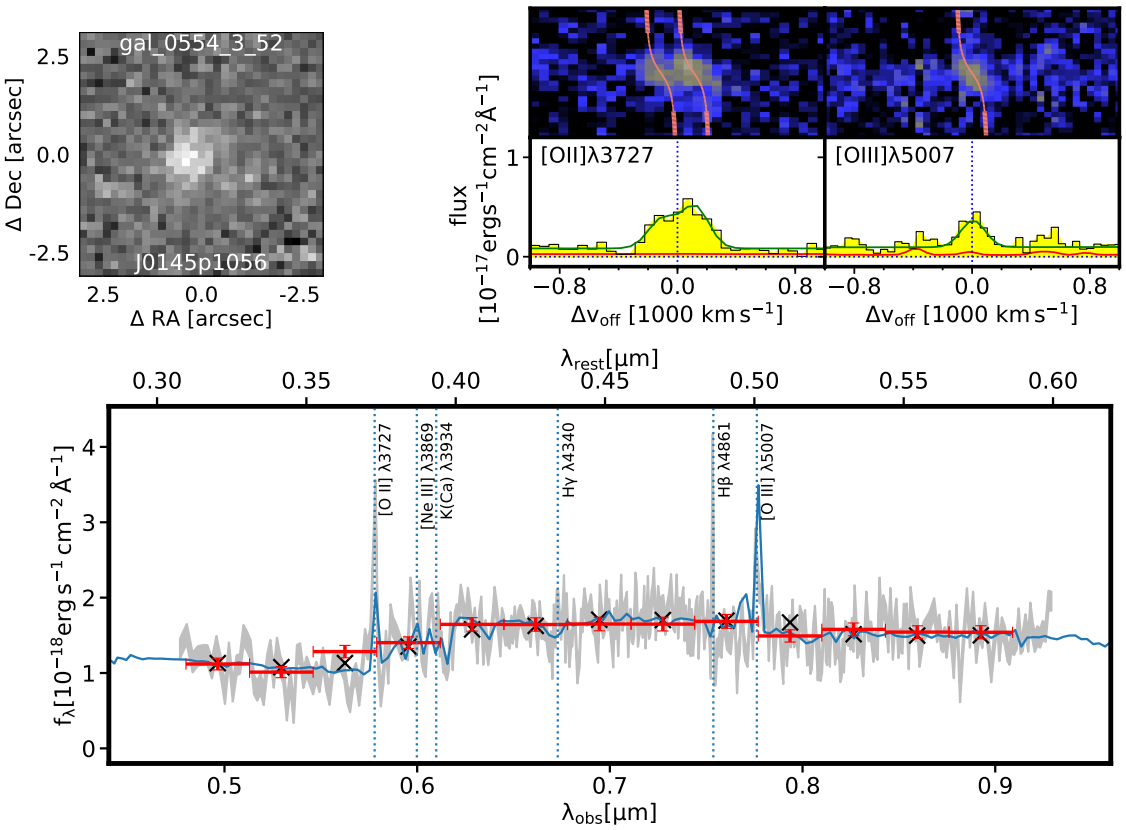

Figure 5. Spectral information of the galaxy gal_J0145p1056_0554_3_52. **Upper left**: [O II] NB image. The image is identical to that shown in Fig. 4. **Upper right**: 1D (bottom) and 2D spectra (top) for both the [O II] doublet and the [O III] λ5007 line. The yellow shaded area in the 1D figures is the extracted aperture spectrum, the green line is the best-fit 1D spectrum, and the red line is the 1σ noise spectrum. Zero velocity is set to the systemic redshift of the galaxy. Dotted vertical and horizontal lines indicate zero velocity and zero flux, respectively. The 2D spectra are pseudo 2D spectra with the virtual slit aligned along the major axis. Over-plotted is the arctan rotation curve as determined from the *GalPak*^{3D} fit (seeing de-convolved). **Lower**: The red error bars show the flux-densities measured with *GALFIT* in the 13 boxcar medium-band filters. The horizontal width of the bars indicates the width of the filter. The blue curve is the best-fit SED obtained from fitting to these filters and the black crosses indicate the filter-averaged flux-densities of this SED. The 1D spectrum extracted from apertures is shown as a grey line, with its vertical width indicating the 1σ uncertainty. For this plot, this spectrum was binned into bins with the same S/N using weighted re-binning (not flux conserving). In addition, it was corrected to total fluxes using the ratios between the *GALFIT* fluxes. More precisely, we used a straight line fit through the measured ratios for all 13 filters in order to estimate a linear wavelength dependence of the aperture loss.

Field ID (1)	Gal ID (2)	z (3)	b (4)	α (5)	i (6)	$r_{\rm half}$ (7)	$r_{\rm turn}$ (8)	$v_{\rm max}$ (9)	σ_0 (10)	$f_{[\rm OII]}$ (11)
J0103p1332	gal_0788_3_25	0.7882	20	4±7(7)	76±6(7)	1.09±0.27	0.98±0.17	46±13(14)	44±2	7.7±0.1
J0145p1056	gal_0554_3_52	0.5500	22	16±7(7)	44±7(7)	2.90±0.27	0.76±0.47	164±35(39)	11±10	4.4±0.2
J0800p1849	gal_0608_10_108	0.6082	65	7.4±0.4(7)	71.3±0.5(7)	4.51±0.04	1.45±0.12	108±3(11)	33±1	27.0±0.1
J1039p0714	gal_0949_6_324	0.9494	49	5±1(7)	61±1(7)	2.80±0.05	1.03	158±3(16)	43±2	9.2±0.1
J1107p1021	gal_1048_5_359	1.0481	41	27±2(7)	78±3(7)	7.00±0.29	3.70±0.44	189±8(21)	3±4	4.4±0.1
J1236p0725	gal_0912_2_246	0.9128	17	22±2(7)	60±3(7)	3.41±0.10	1.24	232±7(24)	8±5	8.8±0.1
J1358p1145	gal_1418_3_291	1.4171	30	10±1(7)	65±1(7)	4.02±0.05	1.15±0.91	8±2(2)	48±1	14.1±0.1
J1509p1506	gal_1046_2_351	1.0469	13	32±3(7)	83±5(7)	3.29±0.21	0.89±0.30	134±10(17)	4±5	7.0±0.2
J2152p0625	gal_1053_6_57	1.0530	49	6±1(7)	74±1(7)	4.88±0.08	0.78±0.08	177±3(18)	2±2	11.0±0.2

Table 4. Kinematical and morphological measurements as obtained from fitting to the [O II] $\lambda\lambda$3727, 3729 doublet with *GalPak*^{3D}. (1) Field ID; (2) Galaxy ID; (3) Galaxy redshift; (4) Impact parameter [kpc]; (5) Azimuthal angle [°]; (6) inclination [°]; (7) half-light radius [kpc]; (8) Turnover radius [kpc]; for the two galaxies without error bar $r_{\rm turn}$ was fixed to $\approx r_{\rm half}/2.7$; (9) Intrinsic maximum rotation velocity $v_{\rm max}$ [km s^{-1}]; (10) Velocity dispersion from turbulence σ_0 [km s^{-1}]; (11) Integrated [O II] flux from the *GalPak*^{3D} model [10^{-17} erg s^{-1} cm^{-2}].

Note. The errors (±) are the statistical 1σ Bayesian uncertainties from *GalPak*^{3D} increased by 20%. For the three parameters used in this paper ($v_{\rm max}$, i and α) we list in parenthesis the total uncertainty, which includes systematics (see §A of the Supplementary Appendix).

of 1D spectra extracted from the cubes using the *MPDAF* routine *extract_spectra*. The spatial extent used for these extractions was set by the extent of the sources as determined by *SExtractor* from the 'optimized' NB images (see §4.1). From these 1D source spectra, we *simultaneously* fit all strong rest-frame emission lines available in the wavelength range covered by the MUSE spectra with a custom MCMC based algorithm that takes into account the spectral FWHM as parametrised by Guérou et al. (2017). The simultaneous fit also allows us to robustly determine the [O II] doublet ratio, but we keep the [O III]λ5007/[O III]λ4959 fixed to 2.98 (as expected theoretically: Storey & Zeippen 2000). The fit results for [O II] and the second brightest line in the MUSE wavelength range other than [O II] are shown in Fig. 5 and Figs. B1 to B8 of the Supplementary Appendix.

The second comparison method is a visual inspection of (pseudo-)2D spectra, which we refer to as position velocity diagrams (PVDs). These PVDs were extracted from the MUSE cubes using a pseudo slit, with the slit aligned along the morpho-kinematic major axis of each galaxy, shown in Fig. 5 and Figs. B1 to B8 of the Supplementary Appendix for each galaxy. We carried out this visual redshift determination for [O II] λ3729 and, if available also for [O III] λ5007.

For the first (second) method, the velocity difference with respect to the redshifts from *GalPak*^{3D} is -1±12 km s^{-1} (5±15 km s^{-1}), respectively, with a maximum difference of 22 (40) km s^{-1}. The individual values are listed in Table C3 of the Supplementary Appendix.

5.2 Photometry and stellar masses

In order to determine continuum photometric magnitudes from the MUSE data, and perform spectral energy distribution (SED) fitting, we determined for each of the galaxies photometry in 13 pseudo medium bands covering the wavelength range from 4800 Å to 9090 Å. Here, instead of creating simple aperture photometry, we determined total magnitudes using *GALFIT* (Peng et al. 2010), which provides two advantages. First, *GALFIT* can simultaneously fit neighbouring or blended galaxies (foreground or background galaxies) and thus remove this contamination, and second it provides a total flux measurement, i.e. is a natural way to take into account the wavelength dependence of the PSF.

For the main galaxies, we assumed a fixed Sersic index of $n = 1$ (exponential). Once we had a satisfying model, we ran *GALFIT* with this model on the medium band filters, allowing only the fluxes to vary. We assumed for each band a Moffat PSF with parameters and wavelength dependence as determined for the quasar (see 3.1.2).

The statistical uncertainties on the flux-densities obtained by the *GALFIT* fit are very small. In order to crudely account for systematic uncertainties in the *GALFIT* modelling, we added a somewhat arbitrary systematic 5% relative uncertainty to the flux-densities.

For the SED fitting, we used a custom SED fitting code *conjecto* (Zabl et al. 2016). As input we used BC03 models (Bruzual & Charlot 2003) with exponential SFHs and nebular line and continuum emission added following the recipe by Schaerer & de Barros (2009) and Ono et al. (2010). Here, we use a Chabrier (2003) IMF and a Calzetti et al. (2000) extinction law. While we used the same extinction law both for nebular and stellar emission, we assumed higher nebular extinction $E_N(B-V)$, than stellar extinction, $E_S(B-V)$ ($E_S(B-V) = 0.7\,E_N(B-V)$). We omit in the following the suffix 'N' and use $E(B-V)$ for the nebular extinction throughout.

The stellar masses, M_*, $E(B-V)$, instantaneous SFRs, and rest-frame B magnitude as obtained from the SED fitting are listed in Table 5. The primary galaxies in our sample cover a relatively small mass range, with all galaxies around $\log(M_*/M_\odot) \approx 10.0 \pm 0.5$.

5.3 [O II] Fluxes and Star formation rates

The only strong emission line we have access to for all of our galaxies is [O II] due to the wavelength coverage of MUSE. Therefore, we need to rely on the observed [O II] luminosity, $L_{[O II];o}$, as our main SFR indicator. The main problem with having only $L_{[O II];o}$ as SFR indicator is the lack of knowledge about the extinction.

In order to get an approximate estimate for the extinction, one could take advantage of the correlation between the star-formation indicator $L_{[O II]}$ itself and $E(B-V)$ (e.g. Kewley et al. 2004) which is equivalently to a SFR$-E(B-V)$ correlation. However, given that the Kewley et al. (2004) relation was determined at $z = 0$ and that the $M_\star-$SFR main-sequence (e.g. Brinchmann et al. 2004; Noeske et al. 2007; Salim et al. 2007) evolves strongly with redshift (e.g. Elbaz et al. 2007; Whitaker et al. 2014; Speagle et al. 2014; Ilbert et al. 2015; Boogaard et al. 2018), it might be better to use the $M_\star - E(B-V)$ relation instead. Indeed, the SFR–$E(B-V)$ relation does strongly depend on redshift (e.g. Sobral et al. 2012), while the $M_\star - E(B-V)$ relation seems to have little or no evolution with redshift (e.g. Sobral et al. 2012; Kashino et al. 2013; Cullen et al. 2017; McLure et al. 2018), indicating $E(B-V)$ is determined by $M_\star$.

Hence, we use the $z = 0$ $M_* - E(B-V)$ relation [14] from Garn & Best (2010), corrected to a Chabrier (2003) IMF:

$$E(B-V) = (0.93 + 0.77\,X + 0.11\,X^2 - 0.09\,X^3)/k_{H\alpha} \quad (1)$$

Here $X = \log(M/M_\odot) - 10$ and $k_{H\alpha} = 3.326$ for the Calzetti et al. (2000) extinction law, both assumed by Garn & Best (2010) and in this study. Garn & Best (2010) state an intrinsic scatter in this relation of about 0.3 dex for the extinction at Hα ($A_{H\alpha}$). Therefore, we include a systematic error of $0.3\,\mathrm{dex}/k_{H\alpha}$ in the error budget for $E(B-V)$.

Another way to get an estimate for the $E(B-V)$ is through SED fitting (§5.2). Both the mass based and the SED based $E(B-V)$ estimates are listed in Table 5. While for most of the galaxies the two $E(B-V)$ values agree within the uncertainties, there are a few cases where the SED based estimates are significantly higher (*J1509*, *J1039*).

Using the assumed extinction curve and the estimated $E(B-V)$ from Eq. (1) we can then de-redden the observed [O II] luminosity to estimate the intrinsic luminosity, $L_{[O II];i}$ assuming a Calzetti et al. (2000) curve. The SFR can then be estimated using the calibration from Kewley et al. (2004):

$$\mathrm{SFR}([O II]) = 4.1 \times 10^{-42} (L_{[O II];i}/\mathrm{erg\,s^{-1}})\,M_\odot\ \mathrm{yr}^{-1} \quad (2)$$

[14] Alternatively, one could correct the $z = 0$ Kewley et al. (2004) $L_{[O II];i} - E(B-V)$ relation by taking into account the MS redshift evolution (SFR $\propto (1+z)^\alpha$; with $\alpha \approx 2-3$).

	ID	$E_{\rm Mass}(B-V)$	$E_{\rm SED}(B-V)$	$\rm SFR_{[OII];2}$	$\rm SFR_{[OII];3}$	$\rm SFR_{SED}$	M_*	$\delta(MS)$	$S05$	B
	(1)	(2)	(3)	(4)	(5)	(6)	(7)	(8)	(9)	(10)
	J0103p1332	$0.22^{+0.09}_{-0.12}$	$0.00^{+0.68}_{-0.00}$	$3.1^{+0.7}_{-0.9}$	$0.9^{+1.5}_{-0.0}$	$0.8^{+26.7}_{-0.0}$	$9.8^{+0.0}_{-0.4}$	$0.18^{+0.52}_{-0.11}$	55 ± 6	-19.6
	J0145p1056	$0.23^{+0.10}_{-0.09}$	$0.26^{+0.29}_{-0.09}$	0.8 ± 0.2	$0.9^{+0.6}_{-0.2}$	$1.5^{+4.3}_{-0.5}$	$9.8^{+0.3}_{-0.1}$	$-0.35^{+0.17}_{-0.19}$	117 ± 27	-19.2
	J0800p1849	0.18 ± 0.09	$0.09^{+0.20}_{-0.01}$	4.6 ± 1.0	$2.7^{+1.3}_{-0.1}$	$1.4^{+3.0}_{-0.0}$	$9.5^{+0.2}_{-0.0}$	$0.60^{+0.12}_{-0.16}$	83 ± 7	-20.0
	J1039p0714	0.21 ± 0.09	$0.77^{+0.04}_{-0.10}$	5.5 ± 1.2	$112.3^{+9.3}_{-26.9}$	$110.2^{+20.1}_{-53.2}$	$9.7^{+0.1}_{-0.0}$	$0.41^{+0.12}_{-0.14}$	120 ± 11	-20.6
	J1107p1021	$0.28^{+0.12}_{-0.10}$	$0.26^{+0.18}_{-0.03}$	$4.9^{+1.4}_{-1.1}$	$4.3^{+1.8}_{-0.3}$	$6.5^{+9.5}_{-1.0}$	$10.0^{+0.3}_{-0.1}$	$0.06^{+0.26}_{-0.21}$	134 ± 14	-20.6
	J1236p0725	$0.39^{+0.18}_{-0.09}$	$0.64^{+0.70}_{-0.00}$	$12.8^{+5.4}_{-2.7}$	$48.8^{+79.8}_{-0.5}$	$7.1^{+680.4}_{-0.0}$	$10.5^{+0.5}_{-0.0}$	$0.14^{+0.15}_{-0.24}$	164 ± 17	-20.8
	J1358p1145	$0.26^{+0.12}_{-0.11}$	$0.26^{+0.10}_{-0.07}$	$29.9^{+8.2}_{-7.7}$	$28.9^{+6.5}_{-4.6}$	$27.8^{+44.9}_{-4.6}$	9.9 ± 0.3	$0.78^{+0.39}_{-0.22}$	48 ± 1	-22.0
	J1509p1506	0.14 ± 0.09	$0.60^{+0.05}_{-0.12}$	3.7 ± 0.8	$43.2^{+5.5}_{-12.1}$	$38.6^{+14.9}_{-18.9}$	$9.3^{+0.2}_{-0.1}$	$0.51^{+0.15}_{-0.17}$	95 ± 12	-20.2
	J2152p0625	$0.34^{+0.12}_{-0.10}$	$0.43^{+0.15}_{-0.14}$	$16.8^{+4.8}_{-3.8}$	$27.3^{+9.6}_{-8.9}$	$22.1^{+28.6}_{-11.0}$	$10.2^{+0.3}_{-0.1}$	$0.39^{+0.23}_{-0.21}$	125 ± 13	-21.2

Table 5. Physical parameters of the galaxies as obtained from the [OII] emission line fluxes and SED fitting. (2) Nebular $E(B-V)$ estimated from stellar mass (Eq. (1)); (3) nebular $E(B-V)$ as obtained from SED fitting (see §5.2); (4) [O II] based SFR [$\rm M_\odot\ yr^{-1}$] from Eq. (2) and assuming $E_{\rm Mass}(B-V)$ as extinction; (5) Same as in 4, but using $E_{\rm SED}(B-V)$ as extinction estimate; (6) Instantaneous SFR [$\rm M_\odot\ yr^{-1}$] directly from SED fit; (7) Stellar mass [$\log_{10}(\rm M_\odot)$] from SED fit; (8) Distance from the Main Sequence ($\log(\rm sSFR(\mathit{Obs})/sSFR(\mathit{MS})$). The observed sSFR was calculated using columns 4) and 7); (9) $S_{0.5} = (0.5 v_{\rm max}^2 + \sigma_0^2)^{0.5}$ [km $\rm s^{-1}$] (10) rest-frame B absolute magnitude calculated from best fit-SED model [mag].

The version here is adjusted with respect to the original version in Kewley et al. (2004) to convert from the Salpeter IMF to the Chabrier IMF assumed here. The obtained SFRs estimates, both using the $E(B-V)$ from Eq. (1) and the $E(B-V)$ from the SED fit are listed in Table 5.

Based on these SFR and M_* (§5.2) estimates we assessed whether we selected typical star-forming galaxies on the SFR-M_* main-sequence (MS). We list for each of our galaxies in Table 5 the distance from the MS, $\delta(MS)$, which is defined as the difference of the logarithms of the measured and expected specific star formation rates (sSFR=SFR/M_*) based on the MS parametrisation by Boogaard et al. (2018) (their eq. 11). Further we show the position of the galaxies in the SFR-M_* plane in Fig. D3 of the Supplementary Appendix. While two galaxies have SFRs elevated compared to the ≈ 0.4 dex scatter of the MS, the seven other galaxies are within the scatter. In addition, it appears that eight out of the nine galaxies are slightly above the MS, which might be significant. However, the assessment of the significance of this trend must take into account all selection effects and this is beyond the scope of the present paper and will be part of the MEGAFLOW survey publication.

5.4 Halo properties

The interpretation of the kinematics of the circumgalactic gas requires an estimate of the properties of the dark matter halos through which the gas moves. We determine the halo masses of our galaxies using two different methods. First, we use the stellar–halo mass relation as obtained from abundance matching by e.g. Behroozi et al. (2010). Second, we derive halo mass estimates from the galaxy kinematics. From the halo masses, we will then compute virial radii.

Using the stellar masses derived in §5.2, and the $z = 1$ stellar–halo mass relation from Behroozi et al. (2010), the halo masses of our galaxies range from $M_{\rm vir} \approx 3\times10^{11} - 3\times10^{12}$ $\rm M_\odot$, covering a range starting from about 1 dex smaller than the halo of a $\rm L^*$ galaxy. Using an estimate for the halo's virial velocity $v_{\rm vir}$ from $v_{\rm max}$, $v_{\rm vir} = v_{\rm max}/(1.1 \pm 0.3)$ as motivated by Dutton et al. (2010) (cf. also Reyes et al. 2012; Cattaneo et al. 2014) we calculate the virial mass of the halos

ID	$v_{\rm vir}$	$M_{\rm vir}$	$M_{\rm vir;abund.}$	$r_{\rm vir}$	r_s
(1)	(2)	(3)	(4)	(5)	(6)
J0103	121^{+17}_{-18}	11.1 ± 0.4	11.6 ± 0.2	128^{+18}_{-19}	20 ± 4
J0145	149^{+66}_{-48}	12.0 ± 0.5	$11.7^{+0.2}_{-0.1}$	189^{+84}_{-60}	27^{+17}_{-11}
J0800	98^{+38}_{-23}	11.4 ± 0.4	$11.5^{+0.2}_{-0.1}$	119^{+46}_{-28}	15^{+8}_{-5}
J1039	143^{+56}_{-34}	11.8 ± 0.4	$11.6^{+0.2}_{-0.1}$	136^{+53}_{-32}	23^{+12}_{-7}
J1107	172^{+67}_{-41}	12.0 ± 0.4	11.8 ± 0.2	153^{+60}_{-37}	29^{+15}_{-9}
J1236	211^{+82}_{-50}	12.3 ± 0.4	$12.2^{+0.4}_{-0.2}$	205^{+80}_{-49}	39^{+20}_{-12}
J1358	152^{+29}_{-21}	$10.9^{+0.4}_{-0.3}$	11.8 ± 0.2	108^{+20}_{-15}	23^{+5}_{-4}
J1509	121^{+48}_{-30}	11.6 ± 0.4	11.4 ± 0.1	108^{+43}_{-27}	19^{+10}_{-6}
J2152	161^{+63}_{-38}	11.9 ± 0.4	$12.0^{+0.3}_{-0.2}$	142^{+55}_{-34}	27^{+14}_{-8}

Table 6. Properties of the host halos (2) Virial velocity [km $\rm s^{-1}$]; For all galaxies except *J0103* and *J1358* identical to $v_{\rm max}/1.1$; For the latter galaxies derived from 4); (3) Viral mass [$\log_{10}(\rm M_\odot)$] from eq. 3 using 2); for *J0103* and *J1358* using $v_{\rm vir}$ estimate based on Burkert et al. (2010) correction for pressure support; (4) Halo mass [$\log_{10}(M_\odot)$] estimated using the stellar–halo mass relation (Behroozi et al. 2010); The uncertainties include both the uncertainties on the stellar mass and the scatter in the stellar–halo mass relation; (5) virial radius [kpc] (cf. §5.4); (6) NFW scale radius [kpc] (cf. §5.4.)

of our galaxies with:

$$M_{\rm vir} = v_{\rm vir}^3 \left(\frac{\Delta_{\rm vir}}{2}\right)^{-0.5} \frac{1}{GH(z)} \tag{3}$$

where the over-density $\Delta_{\rm vir}$ is defined as the ratio between the average matter density within the halo's virial radius and the critical density at the considered redshift and can be approximated as $\Delta_{\rm vir} = 18\pi^2 + 82x - 39x^2$ (Bryan & Norman 1998) with $x = \Omega_m(z) - 1$, for a flat Universe.

Both the abundance matching based halo estimate, $M_{\rm vir;abund.}$, and the dynamical estimate, $M_{\rm vir}$, are listed in Table 6. Apart from *J0103* and especially *J1358*, the agreement between the two estimates is generally good (for a visual comparison see Fig. D1 in the Supplementary Appendix).

The two outliers can be explained. When using the $v_{\rm max}$ measured from the galaxies, we make the assumption that the rotation velocity v_ϕ corresponds to the rotational velocity of the halo $v_{\rm circ}$, where $v_{\rm circ}$ is defined through $M_h(<r) = \frac{r\, v_{\rm circ}^2(r)}{G}$. The assumption $v_{\rm circ} = v_\phi$ will not be

ID (1)	$v_{\rm peak}$ (2)	v sign (3)	$EW_{0;\rm MgII}$ (4)	$EW_{0;\rm MgI}$ (5)	$EW_{0;\rm FeII}$ (6)
J0103	-52	-1	1.1	0.2	0.5
J0145	112	1	0.5	0.1	0.1
J0800	23	1	0.8	0.1	0.3
J1039	-144	-1	0.8	0.2	0.4
J1107	60	-1	0.4	0.1	0.2
J1236	-41	-1	2.1	0.7	1.6
J1358	62	1	2.6	0.5	1.9
J1509	-116	-1	1.5	0.3	1.0
J2152	63	-1	0.6	0.1	0.2

Table 7. Absorber properties. (2) Velocity at peak absorption with respect to systemic redshift [km s^{-1}]. For details see §5.5. (3) Sign of the galaxy rotation field at the position of the quasar sight-line. (4-6) EW_0 for MgII λ2796, MgI λ2853, FeII λ2600, respectively [Å].

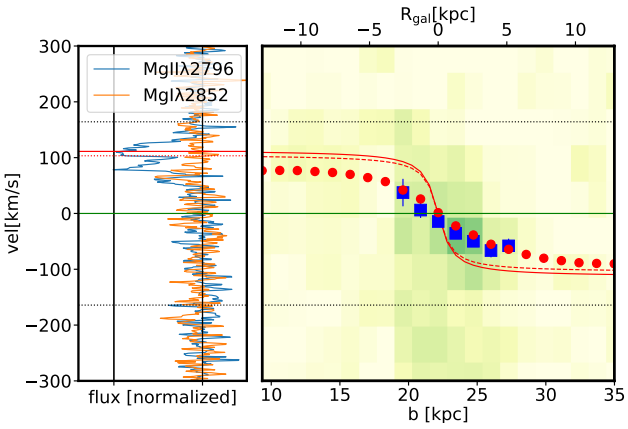

Figure 6. Comparison of galaxy and absorber kinematics at the example of *J0145*. **Identical plots for all nine galaxy-absorber pairs are available in Fig. D2 of the Supplementary Appendix.** The **right panel** shows the 1D galaxy rotation curve (blue points) obtained from the 2D PVD diagram (shown as background image) on the [OII] doublet (see §6.1). The red points are obtained by reproducing this measurement procedure on the seeing convolved best-fit *GalPak*^{3D} model. The solid red line represents the intrinsic *GalPak*^{3D} rotation curve along the galaxy major-axis. The dashed red line represents the modeled rotation curve along the line connecting the galaxy and quasar positions on the sky. The lower x-axis represents the distance b from the quasar along this connecting line. The upper x-axis shows the galacto-centric distance along the galaxy's major axis. In the **left panel** the MgII λ2796 and MgI λ2852 absorption profiles are shown on the same velocity scale as the galaxy rotation curve. The solid red line in this panel indicates $v_{\rm max}$ at the observed inclination, which is a continuation of the red curve in the right panel. Similarly, the red dashed line is the continuation of the rotation curve along the galaxy-quasar axis. Further, the black dotted line shows $v_{\rm max}$ at $incl = 90°$ and the green line is the systemic redshift as obtained from *GalPak*^{3D} ($v = 0$ km s^{-1}).

correct if the galaxies have substantial pressure support as discussed in Burkert et al. (2010, 2016). And indeed, the two galaxies with the largest discrepancy between the two halo estimates, are the two galaxies in our sample with substantial pressure support, as *J0103* has $v/\sigma_0 \approx 1$, while *J1358* has a even more extreme $v/\sigma_0 = 0.3$. Therefore, the approximation of $v_{\rm vir} = v_{\rm max}/1.1$ might not be appropriate in these cases.

Using the pressure support correction from (Burkert et al. 2010) to estimate $v_{\rm circ}$, where $v^2_{\rm circ}(r) = v_\phi(r)^2 + 3.3567\sigma^2(r) \times (r/r_{\rm half})$, evaluated at $r_{\rm half}$ and assuming $v_{\rm vir} = v_{\rm circ}/1.1$, leads indeed to an estimate of $M_{\rm vir}$ which is in much better agreement with the estimate based on the stellar mass. For the remainder of the analysis, we use for *J0103* and *J1358* the abundance matching estimates for $M_{\rm vir}$ and calculated the corresponding $r_{\rm vir}$ and $v_{\rm vir}$. We use the $v_{\rm max}$ based estimates for the other seven galaxies.

Finally, from our virial mass estimates, we determine the virial radius, $r_{\rm vir}$ (and the scale radius r_s for an NFW profile) for the halos. The virial radius, $r_{\rm vir}$, is related to $M_{\rm vir}$ through $M_{\rm vir} = \frac{4\pi}{3}\Delta_{vir}\rho_{\rm crit}r^3_{\rm vir}$. The scale radius, r_s, can be obtained from $r_{\rm vir}$, by making use of the tight relation between $M_{\rm vir}$ or $r_{\rm vir}$ and r_s (e.g. Navarro et al. 1996; using here the version of Diemer & Kravtsov 2015 and making the conversion with their *Colossus* code [15]). The resulting radii are listed in Table 6.

5.5 Absorber kinematics

For the purpose of our work, we need an estimate of a 'characteristic' velocity of the absorbing gas with respect to the systemic redshift defined by the primary galaxy. In practice, we use here the velocity where the optical depth is maximum. The caveat here is that MgII is for most cases saturated and hence the MgII absorption profiles do not allow us to find the peak absorption velocity. Therefore, we used the unsaturated MgI λ2852 line to measure the peak optical depth, except for *J0145*. In this case the MgI line is too weak and we could use here the (nearly) unsaturated MgIIλ 2796 line.

The absorption profiles as obtained from the normalised UVES spectra are shown both for MgII λ2796 and MgI λ2852 in the left panels of Fig. 6 and Fig. D2 of the Supplementary Appendix. The peak absorption velocities are listed in Table 7, where we also list rest-frame equivalent widths for MgII λ2796, MgI λ2852, and FeII λ2600.

As mentioned in §4.3, the *J1039* galaxy-absorber pair at $z = 0.9494$ is somewhat complicated by the presence of another galaxy at 72 kpc, i.e. 1.5 times the impact parameter of the primary galaxy. Interestingly, the absorption system has two distinct components: a weaker one ($EW_0^{\lambda2796} \approx 0.2$Å) from -40 to 10 km s^{-1} and a stronger one ($EW_0^{\lambda2796} \approx 1.0$Å) from -80 to -224 km s^{-1} (Fig. D2). Given the anti-correlation between impact parameter and $EW_0^{\lambda2796}$(e.g. Chen et al. 2010; Nielsen et al. 2013b), it is more likely that the stronger component originates from the 'primary' galaxy's extended gas disk and the weaker component is due to an outflow from the more distant galaxy, as further discussed in Schroetter et al. (in prep).

A further complication for this absorption system is that MgI λ2852 is contaminated by MgII λ2796 of an absorber at $z = 0.9875$. Using the profile shape from the isolated MgII λ2803 of the $z = 0.9875$ system, we could conclude that the MgI peak absorption of the $z = 0.9494$ absorber is the reddest peak within the velocity range covered by the strong MgII component.

Finally, there is also a complication for the MgI λ2852

[15] Available at https://bitbucket.org/bdiemer/colossus.

absorption of *J1358*. At an observed wavelength of 6897 Å it is in a wavelength region strongly affected by telluric absorption. We used the *molecfit* software (Smette et al. 2015; Kausch et al. 2015) to create a model telluric transmittance spectrum in the region from 6860 Å to 6940 Å. Then we divided the science spectrum by this model telluric transmission. The MgI spectrum shown in Fig. D2 is the telluric corrected version.

6 LINE-OF-SIGHT KINEMATICS IN COMPARISON TO GALAXY KINEMATICS

With our sample of nine galaxies geometrically selected to be likely to probe extended disk-like structures (cf. §4.3), we now perform a direct comparison between galaxy and absorber kinematics in order to investigate the existence and properties of a large gaseous structure. In §6.1, we qualitatively compare the MgII and MgI absorptions with the galaxy kinematics. In §6.2, we make a quantitative comparison of the absorption kinematics with simple models for the kinematics of an extended gaseous structure with no radial motion. In §6.3, we discuss the absorption kinematics adding a radial component. In §6.4, we discuss the implication for the angular momentum. Finally, in §6.5 we discuss crude estimates of the accretion rates onto our galaxies.

6.1 Comparison of galaxy and absorber kinematics and qualitative test for co-rotation

In order to compare the absorber and galaxy kinematics for each of the nine galaxies in our sample, we show, in Fig. 6 and Fig. D2 of the Supplementary Appendix, the galaxy kinematics in a PVD. The PVD is obtained from a pseudo 2D spectrum including the [OII] doublet where the $x-$axis (upper) represents the projected distance along the galaxy major-axis oriented with the quasar line-of-sight on the left. The y-axis represents the velocity scale set for the [OII] λ3729 line of the doublet, where the zero point of the velocity scale is set by the galaxies' systemic redshift (see §5.1.2). For each galaxy-absorption pair, the absorber kinematics (as discussed in §5.5) is shown in the left parts of the panels.

In the PVDs, the blue solid squares represent the observed rotation curve, where the velocity is measured using a double Gaussian fit on each spatial pixel of the PVD with the *MPDAF* (Piqueras et al. 2017) routine *gauss_dfit*. The red solid circles represent the seeing convolved rotation curve obtained from the $GalPak^{3D}$ model cube exactly in the same way as for the data, i.e. by performing line fitting on a pseudo PVD generated from the cube along the galaxy major-axis. The red solid line represents the seeing corrected, intrinsic, rotation curve obtained from the $GalPak^{3D}$ model (§5.1). The red dashed line represents the intrinsic rotation curve along the axis intercepting the quasar location. As we selected our galaxy-absorber pairs to have $\alpha < 40\,\mathrm{deg}$, this axis and the major axis are typically very close to each other, and solid and dashed rotation curves differ in most cases little from each other. Fig. 6 and Fig. D2 of the Supplementary Appendix show that, qualitatively, the majority of absorbers tends to follow the rotation curve kinematics, i.e. tends to be blue or red-shifted like the rotation curve is for the side towards the quasar location.

In Fig. 7 (upper), we show all the rotation curves and the corresponding absorptions profiles in a single plot. In this figure, we have self-consistently flipped both the $GalPak^{3D}$ rotation curve (represented by the solid lines) and the absorber velocity for those cases where the quasar is on the side of the galaxy where the galaxy velocity field is negative (= blue-shifted). The absorption profile is represented by the grey vertical bar where darker regions indicate more absorption. Fig. 7 (lower) shows essentially the same as the upper panel, with the difference that here the impact parameter and the velocity are scaled by their respective virial values, $r_{\rm vir}$ and $v_{\rm vir}$. In both panels, the stars indicate the peak absorption velocities as defined in §5.5 and listed in Table 7.

From this figure, several important conclusions can be drawn. First and maybe most importantly that the majority of absorbers share the velocity-sign of the galaxy's velocity field. Indeed, seven out of the nine galaxy-absorber pairs in our sample (i.e. all except *J2152* (violet) and *J1107* (cyan) share the velocity sign and hence meet the minimal condition for co-rotation, if we use the peak velocity. This shows that the gas traced by our MgII absorbers is part of co-rotating structures, supporting the basic prediction from a pure co-rotating disk-like structure (e.g Stewart et al. 2013, 2017; Danovich et al. 2015).

This co-rotation is in contrast to the expectation for gas clouds on random orbits. Assuming that the gas is randomly distributed, the probability for 7 or more out of the 9 sight-lines fulfilling the co-rotation criterion is 9%. If we restrict the sample to the four galaxies at $b < 25$kpc, the probability for four out of four sight-lines to be consistent with co-rotation is 6%.

In addition to this velocity sign test, a second order prediction can be tested. The absorption velocities should not exceed $v_{\rm vir}\sin(i)$.[16] Fig. 7(b) shows that, reassuringly, very little absorbing gas exceeds $v_{\rm vir}\sin i$, except *J1039* which has the most absorption with $|v_{\rm los}| > v_{\rm vir}\sin i$.

To better illustrate the global kinematic shift between the absorbing gas and the systemic redshift, we proceed to stack the nine absorption profiles (normalized as in Fig. 7b). The stacked velocity profile are shown in Fig. 8 for MgIIλ2796, MgIλ2852, FeIIλ2600. In this Figure, gas that is co-rotating with the galaxies' velocity fields is indicated in salmon, while gas that is counter-rotating is coloured light-blue. While the co-rotating part is significantly larger than in the counter-rotating part, this figure also shows that there is almost no absorption below $v_{\rm los} = -0.5 v_{\rm vir}\sin i$ in the counter-rotating direction. We will relate these features quantitatively to simple disk models in §6.2.

6.2 Thin disk with pure circular orbits

In the previous section, we have tested, in a relatively general way, whether the gas probed by the low-α sight-lines approximately shares the orientation of the angular momentum

[16] The product $v_{\rm max}\sin(i) \approx v_{\rm vir}\sin(i)$ can be accurately measured even if the inclination itself cannot be well constrained.

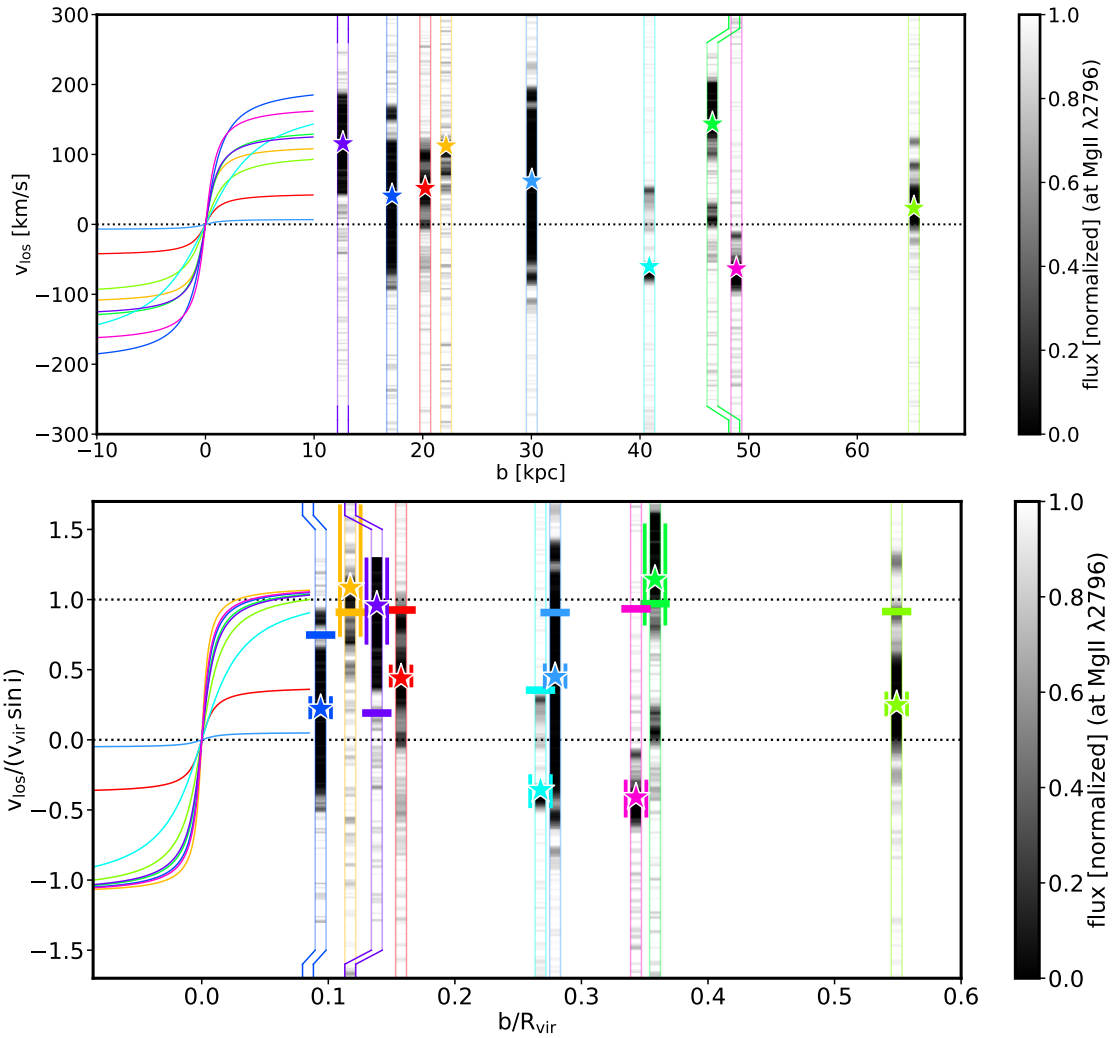

Figure 7. Mg II λ2796 absorption compared to galaxy rotation for each of the nine galaxies-absorber pairs of this study. Galaxy-absorber pairs can be identified by matching colours (as in Table 4). The grey vertical bars represent the Mg II λ2796 profile where the darker regions indicate more absorption, and shifted in the x-direction when they would overlap. The stars indicate the peak of the Mg I profile (see §5.5). The solid lines represent the rotation curves (at the observed inclination), as obtained from the GalPaK^{3D} [O II] fits, and measured along the galaxy major axis. The top panel shows the kinematics as a function of impact parameter b, not galacto-centric distance. The bottom panel shows the same as in the upper panel, but here b and $v_{\rm los}$ have been normalized by $r_{\rm vir}$ and $v_{\rm vir}\,\sin i$, respectively. The coloured bold vertical bars indicate the impact of the uncertainties for $v_{\rm vir}\,\sin i$ on the normalized peak absorption velocity. The coloured horizontal bars indicate the velocity expected from extrapolating the rotating galaxy disk out to the galacto-centric radius of the quasar sight-line assuming a thin disk and rotation with $v_{\rm vir}$.

vector with the host galaxy. Drawing more quantitative conclusions from the line-of-sight (LOS) velocities is difficult, for two main reasons. First, a line-of-sight velocity measurement does not allow one to get the 3D velocity vector of the probed gas. Second, the line-of-sight probes gas at different spatial positions with different velocities. Therefore, quantitative conclusions can only be drawn using a parametrised model for the 3D density and kinematic of the gas.

The simplest possible model is to assume a thin disk which is spatially perfectly co-aligned with the galaxy-disk, meaning that it can be understood as an extension of the galaxy disk. As the galaxy's disk orientation in space - except for an ambiguity in the sign of the inclination - was determined by means of *GalPak*^{3D} modelling, we can predict where the sight-line would cross such a (thin) disk.

A quantitative comparison requires a description of the velocity field from pure rotation at the galacto-centric radius, i.e. the distance from the galaxy centre to the quasar location in the plane of the galaxy. A natural coordinate system is the cylindrical coordinate system (R, ϕ) where the cylinder is perpendicular to the disk. In this system, the radial coordinate is the galacto-centric radius R and ϕ is set arbitrarily to zero along the projected major axis, i.e. $\phi = 0°$ where $\alpha = 0°$. The cylindrical coordinates ϕ and R are related to the azimuthal angle α (introduced in §4.3) and impact parameter b through:

$$\tan\phi = \frac{\tan\alpha}{\cos i} \quad (4)$$

$$R = b(1+\sin^2\alpha\tan^2 i)^{1/2} \quad (5)$$

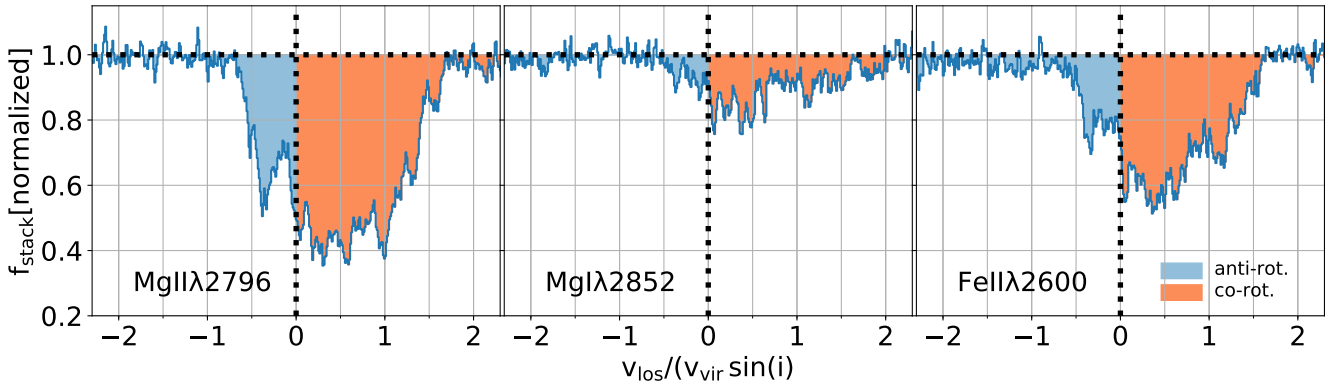

Figure 8. Average absorption profile for our sample of nine galaxy-absorber pairs. The Mg II stack was obtained by calculating the mean of the profiles shown in the lower panel of Fig. 7. The stacks for Mg I and Fe II were obtained in an identical way. As in Fig. 7, for those pairs where the galaxy-rotation was blue-shifted towards the quasar sight-line, we flipped both galaxy and absorber velocities. Consequently, all co-rotation has positive velocities in these stacks (salmon), while all counter-rotating gas has negative velocities (light-blue).

where i is the galaxy inclination. The velocity vector of the gas in the disk plane can then be described as:

$$\boldsymbol{v_{gas}}(\phi, R) \quad = \quad v_\phi(R)\,\hat{\boldsymbol{\phi}}(\phi) \tag{6}$$

where $v_\phi(R)$ is the tangential component of the rotation velocity, i.e. there is no radial flow component and the gas is on (perfect) circular orbits.

Together with the unit vector along the quasar-sight-line, $\boldsymbol{N}$, the line-of-sight component of the velocity field can be determined by this simple linear relation (e.g. Barcons et al. 1995):

$$v_{\rm los} \quad = \quad \boldsymbol{v_{gas}} \cdot \boldsymbol{N} \tag{7}$$

$$\quad = \quad \frac{v_\phi(R)\cos\alpha\sin i}{\sqrt{1+\sin^2\alpha\tan^2 i}} \tag{8}$$

The linear relation between the line-of-sight velocity $v_{\rm los}$ and v_ϕ means that we can either predict the $v_{\rm los}$ for gas with a certain v_ϕ, or alternatively, determine the angular velocity, v_ϕ from a measurement of $v_{\rm los}$ of the gas, if the gas is indeed on perfectly circular orbits in the hypothesized disk.

Eq. (8) shows that the line-of-sight velocity $v_{\rm los}$ will always be smaller than the tangential velocity v_ϕ, i.e. $v_{\rm los} \leq v_\phi$. However, the range of values for the ratio $v_{\rm los}/v_\phi$ can be estimated for the range of allowed values in azimuthal angle α and inclination i imposed by our geometric selection (§4.3). For azimuthal angle $\lesssim 30°$, which corresponds to the range in our sample, and inclinations in the range [40–70°], Eq. (8) implies that $v_{\rm los}$ ranges from 0.5–0.9v_ϕ (= 0.5–1.0 $v_\phi \sin i$). Only for the highest inclinations ($i > 70°$), the range of values becomes very large, essentially from 0.0–1.0v_ϕ, with the sensitivity on the inclination depending on α. In other words, except for extreme inclinations, $v_{\rm los}$ is expected to be 0.5–1.0 $v_\phi \sin i$.

While this range of values is consistent with our observations, this simple model would predict an absorption over a very narrow velocity range at $v_{\rm los}$, whose width would be given by the disk turbulence ($\sim 20-40$ km s^{-1}). In reality, we do not measure a single $v_{\rm los}$, but the absorption profiles (or stacked profile) cover a relatively large range in velocities, from -0.5 to 1.5 $v_{\rm vir}\sin(i)$ (Fig. 8).

One possibility to explain the spread in the absorption profiles is to assume that the hypothesized disk has some thickness (e.g. Steidel et al. 2002; Kacprzak et al. 2010; Ho et al. 2017). In that case, the sight-line intercepts the gaseous disk at different heights, corresponding to different radii R, leading to a range of projected $v_{\rm los}$, even if the gas would be on pure circular orbits with a constant v_ϕ. However, this broadening effect would be a few tens of km s^{-1}, and is not sufficient to explain the range of velocities in Fig. 8.

With the possible caveat of a very thick disk observed at high i, we assume that the peak velocity - the velocity where the optical depth reaches its maximum -, as determined in §5.5, can be used as an estimator for $v_{\rm los}$ at the mid-plane. This line-of-sight velocity $v_{\rm los}$ measured at ϕ and R can then be used to estimate the tangential velocity v_ϕ using Eq. (8).

Note that for sight-lines with large azimuthal angle α (i.e. close to our selection limit of 40°) and for galaxies with very high inclination ($i > 70°$), the galactocentric radius can be very large and very uncertain. This affects especially *J1107* and *J1509*.

This deprojected tangential velocity v_ϕ can then be compared to the circular velocity $v_{\rm circ}$, taken to be $\approx v_{\rm vir}$, in order to assess whether the gas motion is consistent with stable circular orbits. Fig. 9 shows the ratio $v_\phi/v_{\rm vir}$ as a function of the galactocentric radius R (normalized by $r_{\rm vir}$). The error bars are large for *J1107* and *J1509*, as expected from the discussion above. Excluding these two objects, there seems to be a trend with galacto-centric radius, in a sense that galaxies at smaller $R/r_{\rm vir}$ are closer to being on stable circular orbits in the extended galaxy disk.

This trend is also visible by simply looking at the absorption profiles in Fig. 7. We indicate in the lower panel of this Figure the expected $v_{\rm los}$ for circular orbits with $v_{\rm vir}$ at disk-mid plane crossing. While in most cases the peak absorption is not coincident with the expected velocity, there is in many cases at least some absorption at the position of the exact co-rotation.

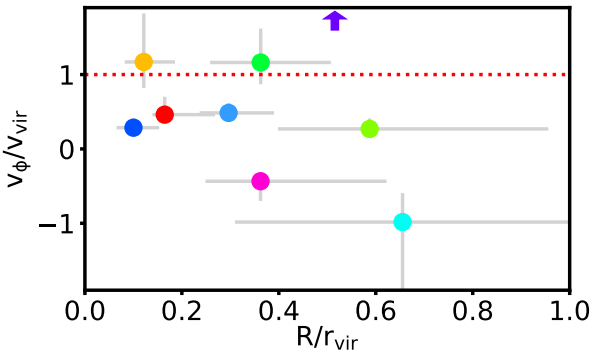

Figure 9. Tangential velocity v_ϕ inferred from v_{los} under the assumption that the gas is on pure circular orbits in the disk plane. For gas on stable circular orbits the expectation is that $v_\phi \approx v_{vir}$. The two cases at the extreme ends of the v_ϕ/v_{vir} distribution (*J1107* cyan; *J1509* purple, indicated by an arrow as outside of plot range) have both the highest α's and inclinations among our nine galaxy-absorber pairs. The values of the plotted points are listed in Table C4 of the Supplementary Appendix.

6.3 Disk with angular and radial motion - Cold accretion disks

While the comparison between galaxy and halo gas absorption velocities for our sample strongly (§ 6.1) indicates that the halo gas probed by the low ionization lines shares at least approximately the direction of the galaxy's angular momentum vector, the previous section showed that the data is in most cases not consistent with the hypothesis that the gas is on stable circular orbits in a perfect extension of the galaxy disks.

Here, we try to gain further insight by extending our thin-disk toy model with a non-zero radial velocity component v_r. The velocity vector of the gas, $\boldsymbol{v_{gas}}$, at a certain position in the disk can then be described by:

$$\boldsymbol{v_{gas}}(\phi, R) = v_\phi(R)\,\hat{\boldsymbol{\phi}}(\phi) + v_r(R)\hat{\boldsymbol{r}}(R), \tag{9}$$

while the observed line-of-sight velocity v_{los} follows (using Eq. (7)):

$$v_{los} = \frac{v_\phi \cos\alpha \sin i + v_r \sin\alpha \tan i}{\sqrt{1+\sin^2\alpha \tan^2 i}}. \tag{10}$$

Unfortunately, removing the constraint of perfect circular orbits and adding the possibility of inflow means that it is no longer possible to infer the velocity vector of the gas from the measured v_{los}, as there are in this scenario two unknowns for one measurement.

However, as discussed in §6.2 for the case of pure circular rotation, we can estimate the range of values for the tangential and radial terms in Eq. (10) imposed by our geometrical selection (§4.3). For the tangential term, the conclusion is similar as in §6.2, i.e. the numerical value ranges from 0.5–0.9 v_ϕ for azimuthal angles $\alpha \lesssim 30°$ and inclinations from 40 to 70°. For the radial term, the absolute value of the numerical factor ranges for this α and i range from 0.0–0.8. Unless the radial velocity $|v_r|$ is *larger* than the tangential component $|v_\phi|$, the tangential component will *typically* dominate the line-of-sight velocity v_{los}, regardless of geometrical factors, except when both i and α are large.

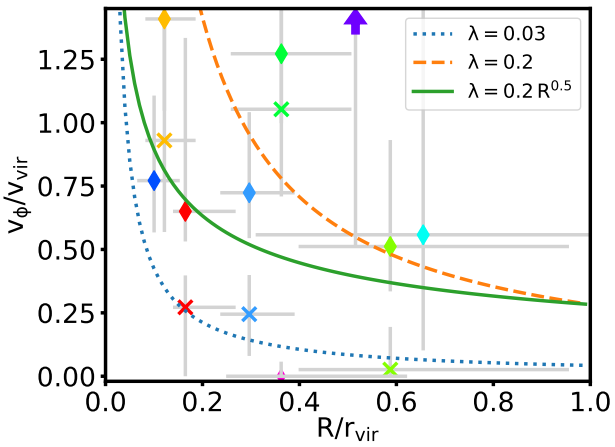

Figure 10. Rotation velocities, v_ϕ, inferred from measured v_{los} under the assumption of a radial velocity component with $v_r = -0.6v_{vir}$ and co-rotation with the galaxy for each of the nine absorbers. There can be up to two solutions per absorber. The projected LOS components of v_r and v_ϕ have the same sign for solutions indicated by stars, while they have opposite signs for solutions indicate by diamonds. The lines indicate different spin parameters (λ, see Eq. (12)), with their values indicated in the legend. The values of the plotted points are listed in Table C4 of the Supplementary Appendix.

In order to break the degeneracy between radial and circular velocity, it is necessary to impose some additional information to reduce the dimensionality. Motivated by results from simulations one justifiable assumption is a constant v_r (e.g. Rosdahl & Blaizot 2012; Goerdt & Ceverino 2015). By measuring v_r directly from different simulations with different codes as a function of radius, redshift, and halo mass, Goerdt & Ceverino (2015) find that typical inflow velocities are approximately constant with radius at $v_r \approx -0.6\,v_{vir}$ for redshift $z \approx 1$.

We now test the impact of the assumption of $v_r = -0.6\,v_{vir}$ and the possible signatures that this would have on our data. Such a radial component means that the magnitude of the radial term in Eq. (10) is thus at most $|v_r| < 0.6\,v_{vir}$, while the tangential component is ≈ 0.5–$0.9\,v_{vir}$, for inclinations less than 70° and $\alpha < 30°$. This implies that disks with such a radial flow allow a wide range of line-of-sight velocities v_{los}, from ≈ 0–$1.1\ v_{vir}$ in most general situations, i.e. except for the most extreme inclinations $i > 70°$, and thus can better reproduce the range of velocities observed in Fig. 8.

Now, we use the v_{los} observations of our individual cases to put constraints on the tangential velocity with the assumption of a radial flow at $v_r = -0.6v_{vir}$. Given that we do not know whether the line-of-sight is crossing the disk on the near or far side, this means the radial contribution to the line-of-sight velocity v_{los} in Eq. (10) can have a sign opposite to the tangential component v_ϕ. Consequently, two solutions can be found depending on the sign of the inclination, i.e.

$$v_{los} = \frac{\mathrm{sign}(v_{rot})|v_\phi| \cos\alpha \sin|i| \pm v_r \sin\alpha \tan|i|}{\sqrt{1+\sin^2\alpha \tan^2 i}}, \tag{11}$$

where the $+(-)$ sign corresponds to whether the quasar intercepts the gaseous disk on the far or near side. Given that

we impose corotation between the gas and host galaxy, i.e. sign(v_ϕ) is given by sign($v_{\rm rot}$), no solution can be obtained, if the $v_{\rm los}$ has the opposite sign as the assumed sign for v_ϕ, and the absolute value of $v_{\rm los}$ is larger than the absolute value of the line-of-sight component from the radial velocity. With Eq. (11), it is possible to have either one, two or no solutions, depending on $v_{\rm los}$.

In Figure 10, we use Eq. (11) to put constraints on v_ϕ for the galaxies in our sample with our assumption of $v_{\rm r} = -0.6 v_{\rm vir}$. The resulting solutions for v_ϕ normalized by $v_{\rm vir}$ are shown as a function of $R/r_{\rm vir}$. Solutions where the $v_{\rm los}$ contribution from $v_{\rm r}$ shares the sign with the contribution from v_ϕ, are indicated as crosses, while solutions where they have the opposite sign are shown as diamonds. A case where the measured value does not give a co-rotating solution, but a co-rotating solution is possible within the uncertainties, is indicated by the small pink diamond at 0.36 for *J2152*.

A first important conclusion from Figure 10 is that, under the assumption of this infall velocity, there is for each absorber at least one solution consistent with $0 < v_\phi/v_{\rm vir} < 1$ in the co-rotating direction, even for the two cases which would in the absence of infall be interpreted to have a counter-rotating circular velocity.

6.4 Consequences for the angular momentum

Using the constraints on the tangential velocity v_ϕ from the previous section, we now analyse the implications for the gas and galaxy angular momentum. Indeed, a crucial aspect for any theory of galaxy evolution is to understand the amount of angular momentum which the accreted gas carries with it. A useful quantity, which expresses the specific angular momentum of the gas, $j = v_\phi R$, in a form independent of the virial parameters, is through the dimensionless spin-parameter, λ. We use the definition of λ from Bullock et al. (2001):

$$\lambda = \frac{1}{\sqrt{2}} \frac{j}{r_{\rm vir} v_{\rm vir}} = \frac{1}{\sqrt{2}} \frac{R}{r_{\rm vir}} \frac{v_\phi}{v_{\rm vir}} \tag{12}$$

Pure N-body simulations have shown that λ of the dark matter component integrated over the halo is approximately distributed with a log-normal distribution with $|\lambda| = 0.035$ and $\sigma = 0.5$, almost independent from redshift and halo mass (e.g. Bullock et al. 2001; Bett et al. 2007). Some hydrodynamical simulations predict that the cold accreting gas should have a higher λ on its way to the galaxy than the dark matter (e.g. Stewart et al. 2011b; Teklu et al. 2015; Danovich et al. 2015). E.g. Danovich et al. (2015), using a similar simulation as Goerdt & Ceverino (2015), predict that the spin parameter λ for the cold gas, which we presumably probe with our data, scales with $(R/r_{\rm vir})^{0.5}$, and has approximately a $\lambda = 0.06$ at $R/r_{\rm vir} = 0.1$ and $\lambda = 0.2$ at $R/r_{\rm vir} = 1.0$.

We indicate in Fig. 10 the curves of constant $\lambda = 0.03$ (blue dotted line) and $\lambda = 0.2$ (orange dashed line). In addition, we show the curve $\lambda = 0.2(R/r_{\rm vir})^{0.5}$ (green solid line). All galaxy-absorber pairs except *J2152* have within the uncertainties at least one solution within $0.03 < \lambda < 0.2$. For most of the absorber pairs a solution with $\lambda = 0.2(R/r_{\rm vir})^{0.5}$ seems plausible, but also a solution with constant $\lambda \approx 0.03$ is consistent with several of the absorbers.

ID	$R/r_{\rm vir}$	$\log_{10}(\cos(i) N_{\rm HI})$	$\dot{M}_{\rm in}(R)$
(1)	(2)	(3)	(4)
J0103	$0.16^{+0.10}_{-0.03}$	18.9±0.5	$0.9^{+2.0}_{-0.6}$
J0145	$0.12^{+0.06}_{-0.04}$	18.6±0.5	$0.7^{+1.5}_{-0.5}$
J0800	$0.59^{+0.37}_{-0.19}$	18.7±0.5	$1.8^{+4.0}_{-1.3}$
J1039	$0.36^{+0.14}_{-0.10}$	18.9±0.5	$2.7^{+6.0}_{-2.0}$
J1107	$0.66^{+1.27}_{-0.35}$	17.9±0.5	$0.7^{+1.8}_{-0.6}$
J1236	$0.10^{+0.05}_{-0.03}$	19.8±0.5	$12.5^{+27.5}_{-9.1}$
J1358	$0.30^{+0.09}_{-0.06}$	19.9±0.5	$17.7^{+38.4}_{-12.3}$
J1509	$0.52^{+1.52}_{-0.33}$	18.8±0.5	$2.2^{+6.5}_{-1.9}$
J2152	$0.36^{+0.26}_{-0.11}$	18.4±0.5	$1.0^{+2.1}_{-0.7}$

Table 8. Accretion measurements (see §6.5) (2) Galacto-centric radius (see Eq. (5)) normalised by virial radius, $r_{\rm vir}$; (3) HI column density perpendicular to disk (based on MgII equivalent width) [cm^{-2}] ; (4) Mass accretion rate [$M_\odot$ yr^{-1}].

6.5 Amount of accretion compared to star formation

Galaxies need to accrete gas from their halo. A plausible reservoir might be the extended cold gas disks probed by our sample. In section 6.3 we have shown that the $v_{\rm los}$ measured for this gas are indeed consistent with infall rates and angular momentum predicted by simulations. Motivated by this, we can estimate the mass accretion rates from the MgII equivalent widths and the assumed infall velocities ($v_{\rm r} = -0.6 v_{\rm vir}$).

For this estimate, first the MgII λ2796 equivalent widths need to be converted to approximate HI column densities using the relation from Ménard & Chelouche (2009):

$$N_{\rm HI} = (2.45 \pm 0.38) \times 10^{19} {\rm cm}^{-2} \left(\frac{EW_0^{\lambda 2796}}{\rm \AA} \right)^{2.08 \pm 0.24} \tag{13}$$

The $EW_0^{\lambda 2796} - N_{\rm HI}$ relation is not a tight relation. We assume in the following an approximate statistical uncertainty of 0.5 dex on the $N_{\rm HI}$ estimates. However, significantly stronger outliers are not unlikely.

Then, the accretion rate, $\dot{M}_{\rm in}(R)$ through a cylinder at the galacto-centric radius R can be calculated as in Bouché et al. (2013):

$$\dot{M}_{\rm in}(R) \approx 2\pi \, R \, v_{\rm r} \, m_p \, \mu \, \cos(i) \, N_{\rm HI} \tag{14}$$

Here the assumption is made that the disk is thin enough so that the column density perpendicular to disk can be estimated from the column density along the inclined view through $\cos(i) N_{\rm HI}$. Further, m_p is the proton mass, and μ is the mean molecular weight, assumed to be 1.6. A further assumption is that all v_ϕ, $v_{\rm r}$, and the perpendicular column density do at fixed galacto-centric radius not depend on the disk azimuthal angle. The resulting $\dot{M}_{\rm in}$ are listed in Table 8.

In Fig. 11, we compare the estimated $\dot{M}_{\rm in}$ to the SFRs computed using the [OII] luminosities with the extinction estimated from the $M_\star$-extinction relation of Garn & Best (2010) as described in §5.3. The dashed line shows the 1:1 relation, and the dotted lines are deviations from the 1:1 relation by a factor five. This figure shows that the estimated amount of $\dot{M}_{\rm in}$ seems sufficient to balance the SFRs. Given that our estimate from Eq. (14) only takes account for the neutral component, the total $\dot{M}_{\rm in}$ could be sufficiently higher

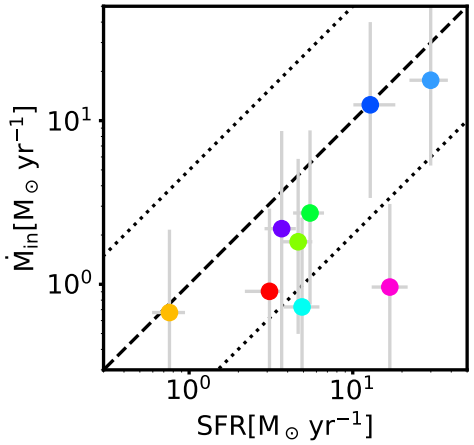

Figure 11. Mass inflow rate estimated from Mg II equivalent width plotted against SFR estimate obtained from [O II] flux corrected for reddening using the $E(B-V)$ estimate based on the Garn & Best (2010) M_*-extinction relation. The dashed line represents a 1:1 relation. The dotted lines represent deviations from the 1:1 correspondence by a factor five.

if an ionised or molecular component would contribute to the inflow.

This result seems consistent with the expectation of self-regulation model (as in Bouché et al. 2010; Lilly et al. 2013) where

$$\mathrm{SFR} = \frac{\epsilon_{\rm in}\, f_B\, \dot{M}_{\rm h}}{1-R+\eta} \approx \frac{\dot{M}_{\rm in}}{1-R+\eta} \qquad (15)$$

where $\epsilon_{\rm in}$ is the accretion efficiency, f_B the baryon fraction, $\dot{M}_{\rm h}$ the halo accretion rate at $r_{\rm vir}$, R the 'recycling fraction' which massive stars return to the ISM, and η the outflow loading factor, $\eta \equiv \dot{M}_{\rm out}/\mathrm{SFR}$. In the mass range for the galaxies in our sample η is measured to be small $\lesssim 1$ (Martin et al. 2012; Schroetter et al. 2015, 2016) and R is around 0.3–0.5 depending on the IMF (e.g. Madau & Dickinson 2014).

7 SUMMARY & CONCLUSIONS

Using our ongoing MEGAFLOW survey (Schroetter et al. 2016, Bouché et al. (in prep.), Schroetter et al. (in prep.)), which targets galaxies around 79 strong Mg II absorbers (with $EW_0^{\lambda 2796} \gtrsim 0.3$Å) at $z \approx 1$ with the VLT/MUSE spectrograph, we have investigated the distribution and kinematic properties of this low-ionization gas. Remarkably, the distribution of the azimuthal angle α for the galaxy-absorbers pairs within 100 kpc shows a clear bi-modality (Fig. 2, top panel), which is highly suggestive of a CGM geometry with biconical outflows and extended gas disks. Our result confirms previous ones by Bouché et al. (2012); Kacprzak et al. (2012) and Bordoloi et al. (2011).

In light of this bimodal distribution, we have selected for this study the nine galaxy-absorber pairs which have the right orientation for the purpose of studying extended gaseous disks at galactocentric distances of 20–100kpc. This is the first statistical sample with both galaxy and absorber kinematics at $z \approx 1$ specifically selected to study the cold gas disks.

Through a comparison of absorber and galaxy kinematics, we derived the following main conclusions:

- There is little gas with $v_{\rm los} > v_{\rm vir}\sin(i)$, which suggests that the gas in the disk is gravitationally bound to the halo. (§6.1; Figs. 7 and 8)
- For seven out of the nine pairs the absorption velocity shares the velocity sign with the extrapolation of the galaxy rotation curve to the position of the quasar. This is the case for all four absorbers at $b/r_{\rm vir} < 0.2$ (§6.1; Fig. 7);
- The inferred rotation velocity using the peak absorption velocity is in many cases smaller than $v_{\rm vir}$. This indicates that the gas is not on purely circular orbits. There seems to be a tendency for the discrepancy to be larger at larger impact parameters, with two cases at $b/r_{\rm vir} > 0.25$ even having counter-rotating velocities (§6.2; Fig. 9);
- We investigated a scenario where the disk gas has a radial inflow (accretion component) in addition to the circular component, as predicted by simulations and required by indirect evidence. We showed that the data are consistent with inflow rates ($v_{\rm r} \approx -0.6 v_{\rm vir}$) and angular momentum distributions (§6.3 & §6.4; Fig. 10) from simulations;
- The inferred accretion rates are consistent with the expectation from the gas-regulator (Bouché et al. 2010; Lilly et al. 2013; Davé et al. 2012) (§6.5; Fig. 11) and from hydrodynamical calculations (e.g. Faucher-Giguère et al. 2011; Nelson et al. 2015; Correa et al. 2018).

For some of the conclusions listed above we needed to make relatively strong assumptions. E.g. we assumed that the gas is in a perfect extension of the galaxy disk and the angular momentum vector of the gas is perfectly aligned with the galaxy. This is not exactly what simulations predict for the cold streams falling into the halo, and only to some extent the case for the cold-accretion disks into which the streams supposedly settle in the inner-halo. In addition, extended gas disks might be warped. While the gas needs to finally align with the galaxy disk, how this alignment happens and out to where it persists is far from a solved question. In simulations it seems to depend on the code and the feedback implementations (e.g. Stewart et al. 2017). However, reassuringly our α histogram shows that the gas that we probe with Mg II needs to be at least in a disky structure.

The finding of gravitationally bound co-rotating gas is consistent with a range of quasar-absorption studies for individual objects with the right geometry ranging up to $z \approx 2$ (e.g. Barcons et al. 1995; Steidel et al. 2002; Bouché et al. 2013, 2016; Bowen et al. 2016; Rahmani et al. 2018). The only other study that systematically selected a statistical sample with the right geometry for the purpose of studying extended cold gas disks was recently performed by Ho et al. (2017). Importantly, their work is targeting galaxies at significantly lower redshift, $z \approx 0.2$, and hence can be considered complementary to our study. Qualitatively they find at this lower redshift a similar result as we do: The majority of the Mg II absorption profiles matches the sign of the galaxy rotation (8 out of their 12 robust galaxy-absorber identifications). Similarly to us, they also find that the majority of the gas has $v_\phi < v_{\rm circ}$. Combining this with the fact that for some systems part of the absorption counter-rotates, they conclude also - for $z \approx 0.2$ - that the gas likely has a radial infall component.

ACKNOWLEDGEMENTS

We thank the anonymous referee for a careful and constructive report, which helped to improve the quality of the manuscript. This work has been carried out thanks to the support of the ANR FOGHAR (ANR-13-BS05-0010- 02), the ANR 3DGasFlows (ANR-17-CE31-0017), the OCEVU Labex (ANR-11-LABX-0060), and the A*MIDEX project (ANR-11-IDEX-0001-02) funded by the "Investissements d'avenir" French government program. LW acknowledges support by the Competitive Fund of the Leibniz Association through grant SAW-2015-AIP-2.

This work made use of the following open source software: GalPak3D (Bouché et al. 2015), ZAP (Soto et al. 2016b), MPDAF (Piqueras et al. 2017), matplotlib (Hunter 2007), NumPy (van der Walt et al. 2011; Oliphant 2007), Astropy (Astropy Collaboration et al. 2013), Montage (**?**).

REFERENCES

Amorisco N. C., Bertin G., 2010, A&A, 519, A47
Astropy Collaboration et al., 2013, A&A, 558, A33
Bacon R., et al., 2006, Msngr, 124, 5
Bacon R., et al., 2010, in Society of Photo-Optical Instrumentation Engineers (SPIE) Conference Series. p. 8, doi:10.1117/12.856027
Bacon R., et al., 2015, A&A, 575, A75
Bacon R., et al., 2017, A&A, 608, A1
Barcons X., Lanzettat K. M., Webb J. K., 1995, Nature, 376, 321
Behroozi P. S., Conroy C., Wechsler R. H., 2010, ApJ, 717, 379
Bergeron J., 1988, in IAU Symp. 130: Large Scale Structures of the Universe. pp 343–+
Bergeron J., Boissé P., 1991, A&A, 243, 344
Bertin E., Arnouts S., 1996, A&AS, 117, 393
Bett P., Eke V., Frenk C. S., Jenkins A., Helly J., Navarro J., 2007, MNRAS, 376, 215
Bigiel F., Leroy A., Seibert M., Walter F., Blitz L., Thilker D., Madore B., 2010, ApJ, 720, L31
Birnboim Y., Dekel A., 2003, MNRAS, 345, 349
Boogaard L. A., et al., 2018, A&A, 619, A27
Bordoloi R., et al., 2011, ApJ, 743, 10
Borisova E., et al., 2016, ApJ, 831, 39
Bosma A., 1981, AJ, 86, 1791
Bouché N. F., 2017, in Fox A., Davé R., eds, Astrophysics and Space Science Library Vol. 430, Gas Accretion onto Galaxies. p. 355 (arXiv:1612.00740), doi:10.1007/978-3-319-52512-9_15
Bouché N., et al., 2010, ApJ, 718, 1001
Bouché N., Hohensee W., Vargas R., Kacprzak G. G., Martin C. L., Cooke J., Churchill C. W., 2012, MNRAS, 426, 801
Bouché N., Murphy M. T., Kacprzak G. G., Péroux C., Contini T., Martin C. L., Dessauges-Zavadsky M., 2013, Science, 341, 50
Bouché N., Carfantan H., Schroetter I., Michel-Dansac L., Contini T., 2015, AJ, 150, 92
Bouché N., et al., 2016, ApJ, 820, 121
Bowen D. V., Chelouche D., Jenkins E. B., Tripp T. M., Pettini M., York D. G., Frye B. L., 2016, ApJ, 826, 50
Brinchmann J., Charlot S., White S. D. M., Tremonti C., Kauffmann G., Heckman T., Brinkmann J., 2004, MNRAS, 351, 1151
Bruzual G., Charlot S., 2003, MNRAS, 344, 1000
Bryan G. L., Norman M. L., 1998, ApJ, 495, 80
Bullock J. S., Dekel A., Kolatt T. S., Kravtsov A. V., Klypin A. A., Porciani C., Primack J. R., 2001, ApJ, 555, 240
Burkert A., et al., 2010, ApJ, 725, 2324
Burkert A., et al., 2016, ApJ, 826, 214
Calzetti D., Armus L., Bohlin R. C., Kinney A. L., Koornneef J., Storchi-Bergmann T., 2000, ApJ, 533, 682
Cappellari M., 2017, MNRAS, 466, 798
Cappellari M., Emsellem E., 2004, PASP, 116, 138
Casuso E., Beckman J. E., 2004, A&A, 419, 181
Cattaneo A., Salucci P., Papastergis E., 2014, ApJ, 783, 66
Chabrier G., 2003, PASP, 115, 763
Chen H.-W., Kennicutt Jr. R. C., Rauch M., 2005, ApJ, 620, 703
Chen H.-W., Helsby J. E., Gauthier J.-R., Shectman S. A., Thompson I. B., Tinker J. L., 2010, ApJ, 714, 1521
Churchill C. W., Rigby J. R., Charlton J. C., Vogt S. S., 1999, ApJS, 120, 51
Churchill C. W., Trujillo-Gomez S., Nielsen N. M., Kacprzak G. G., 2013, ApJ, 779, 87
Coil A. L., Weiner B. J., Holz D. E., Cooper M. C., Yan R., Aird J., 2011, ApJ, 743, 46
Correa C. A., Schaye J., van de Voort F., Duffy A. R., Wyithe J. S. B., 2018, MNRAS, 478, 255
Cullen F., McLure R. J., Khochfar S., Dunlop J. S., Dalla Vecchia C., 2017, MNRAS, 470, 3006
Daddi E., et al., 2010, ApJ, 713, 686
Danovich M., Dekel A., Hahn O., Ceverino D., Primack J., 2015, MNRAS, 449, 2087
Davé R., Finlator K., Oppenheimer B. D., 2012, MNRAS, 421, 98
Dekel A., Birnboim Y., 2006, MNRAS, 368, 2
Dekel A., et al., 2009, Nature, 457, 451
Dekker H., D'Odorico S., Kaufer A., Delabre B., Kotzlowski H., 2000, in Iye M., Moorwood A. F., eds, Proc. SPIEVol. 4008, Optical and IR Telescope Instrumentation and Detectors. pp 534–545, doi:10.1117/12.395512
Di Teodoro E. M., Fraternali F., 2015, MNRAS, 451, 3021
Diamond-Stanic A. M., Coil A. L., Moustakas J., Tremonti C. A., Sell P. H., Mendez A. J., Hickox R. C., Rudnick G. H., 2016, ApJ, 824, 24
Diemer B., Kravtsov A. V., 2015, ApJ, 799, 108
Dutton A. A., Conroy C., van den Bosch F. C., Prada F., More S., 2010, MNRAS, 407, 2
Elbaz D., et al., 2007, A&A, 468, 33
Epinat B., et al., 2012, A&A, 539, A92
Faucher-Giguère C.-A., Kereš D., Ma C.-P., 2011, MNRAS, 417, 2982
Fox A., Davé R., eds, 2017, Gas Accretion onto Galaxies Astrophysics and Space Science Library Vol. 430, doi:10.1007/978-3-319-52512-9.
Freundlich J., et al., 2013, A&A, 553, A130
Fumagalli M., Prochaska J. X., Kasen D., Dekel A., Ceverino D., Primack J. R., 2011, MNRAS, 418, 1796
Garn T., Best P. N., 2010, MNRAS, 409, 421
Genzel R., et al., 2015, ApJ, 800, 20
Goerdt T., Ceverino D., 2015, MNRAS, 450, 3359
Goerdt T., Dekel A., Sternberg A., Gnat O., Ceverino D., 2012, MNRAS, 424, 2292
Guérou A., et al., 2017, A&A, 608, A5
Hayashi M., et al., 2014, MNRAS, 439, 2571
Ho S. H., Martin C. L., Kacprzak G. G., Churchill C. W., 2017, ApJ, 835, 267
Hunter J. D., 2007, Computing In Science & Engineering, 9, 90
Ianjamasimanana R., Walter F., de Blok W. J. G., Heald G. H., Brinks E., 2018, AJ, 155, 233
Ilbert O., et al., 2015, A&A, 579, A2
Kacprzak G. G., 2017, in Fox A., Davé R., eds, Astrophysics and Space Science Library Vol. 430, Gas Accretion onto Galaxies. p. 145 (arXiv:1612.00451), doi:10.1007/978-3-319-52512-9_7
Kacprzak G. G., Churchill C. W., Ceverino D., Steidel C. C., Klypin A., Murphy M. T., 2010, ApJ, 711, 533

Kacprzak G. G., Churchill C. W., Barton E. J., Cooke J., 2011, ApJ, 733, 105
Kacprzak G. G., Churchill C. W., Nielsen N. M., 2012, ApJ, 760, L7
Kamann S., Wisotzki L., Roth M. M., 2013, A&A, 549, A71
Kashino D., et al., 2013, ApJ, 777, L8
Kausch W., et al., 2015, A&A, 576, A78
Kereš D., Katz N., Weinberg D. H., Davé R., 2005, MNRAS, 363, 2
Kewley L. J., Geller M. J., Jansen R. A., 2004, AJ, 127, 2002
Kimm T., Devriendt J., Slyz A., Pichon C., Kassin S. A., Dubois Y., 2011, preprint, (arXiv:1106.0538)
Kreckel K., Peebles P. J. E., van Gorkom J. H., van de Weygaert R., van der Hulst J. M., 2011, AJ, 141, 204
L'Huillier B., Combes F., Semelin B., 2012, A&A, 544, A68
Lan T.-W., Mo H., 2018, preprint, (arXiv:1806.05786)
Lanzetta K. M., Bowen D., 1990, ApJ, 357, 321
Larson R. B., 1972a, Nature Physical Science, 236, 7
Larson R. B., 1972b, Nature, 236, 21
Lehner N., O'Meara J. M., Howk J. C., Prochaska J. X., Fumagalli M., 2016, ApJ, 833, 283
Lilly S. J., Carollo C. M., Pipino A., Renzini A., Peng Y., 2013, ApJ, 772, 119
Lynden-Bell D., 1975, Vistas in Astronomy, 19, 299
Madau P., Dickinson M., 2014, ARA&A, 52, 415
Marino R. A., et al., 2018, ApJ, 859, 53
Martin C. L., Shapley A. E., Coil A. L., Kornei K. A., Bundy K., Weiner B. J., Noeske K. G., Schiminovich D., 2012, ApJ, 760, 127
McLure R. J., et al., 2018, MNRAS, 476, 3991
Ménard B., Chelouche D., 2009, MNRAS, 393, 808
Mignoli M., et al., 2013, A&A, 556, A29
Moffat A. F. J., 1969, A&A, 3, 455
Murphy M. T., 2016, UVES popler: POst-PipeLine Echelle Reduction software, doi:10.5281/zenodo.44765
Muzahid S., Kacprzak G. G., Churchill C. W., Charlton J. C., Nielsen N. M., Mathes N. L., Trujillo-Gomez S., 2015, ApJ, 811, 132
Navarro J. F., Frenk C. S., White S. D. M., 1996, ApJ, 462, 563
Neeleman M., Prochaska J. X., Ribaudo J., Lehner N., Howk J. C., Rafelski M., Kanekar N., 2016, ApJ, 818, 113
Nelson D., Genel S., Vogelsberger M., Springel V., Sijacki D., Torrey P., Hernquist L., 2015, MNRAS, 448, 59
Nielsen N. M., Churchill C. W., Kacprzak G. G., Murphy M. T., 2013a, ApJ, 776, 114
Nielsen N. M., Churchill C. W., Kacprzak G. G., 2013b, ApJ, 776, 115
Nielsen N. M., Churchill C. W., Kacprzak G. G., Murphy M. T., Evans J. L., 2015, ApJ, 812, 83
Nielsen N. M., Churchill C. W., Kacprzak G. G., Murphy M. T., Evans J. L., 2016, ApJ, 818, 171
Noeske K. G., et al., 2007, ApJ, 660, L43
Oke J. B., 1974, ApJS, 27, 21
Oliphant T. E., 2007, Computing in Science Engineering, 9, 10
Ono Y., Ouchi M., Shimasaku K., Dunlop J., Farrah D., McLure R., Okamura S., 2010, ApJ, 724, 1524
Pagel B. E. J., Patchett B. E., 1975, MNRAS, 172, 13
Peng C. Y., Ho L. C., Impey C. D., Rix H.-W., 2010, AJ, 139, 2097
Péroux C., McMahon R. G., Storrie-Lombardi L. J., Irwin M. J., 2003, MNRAS, 346, 1103
Pichon C., Pogosyan D., Kimm T., Slyz A., Devriendt J., Dubois Y., 2011, MNRAS, 418, 2493
Piqueras L., Conseil S., Shepherd M., Bacon R., Leclercq F., Richard J., 2017, preprint, (arXiv:1710.03554)
Prochaska J. X., et al., 2017, ApJ, 837, 169
Putman M. E., et al., 2009, ApJ, 703, 1486
Rahmani H., et al., 2018, MNRAS, 474, 254
Rees M. J., Ostriker J. P., 1977, MNRAS, 179, 541
Reyes R., Mandelbaum R., Gunn J. E., Nakajima R., Seljak U., Hirata C. M., 2012, MNRAS, 425, 2610
Rosdahl J., Blaizot J., 2012, MNRAS, 423, 344
Rubin K. H. R., 2017, in Fox A., Davé R., eds, Astrophysics and Space Science Library Vol. 430, Gas Accretion onto Galaxies. p. 95 (arXiv:1612.00805), doi:10.1007/978-3-319-52512-9_5
Rubin K. H. R., Prochaska J. X., Koo D. C., Phillips A. C., 2012, ApJ, 747, L26
Saintonge A., et al., 2013, ApJ, 778, 2
Saintonge A., et al., 2016, MNRAS, 462, 1749
Saintonge A., et al., 2017, ApJS, 233, 22
Salim S., et al., 2007, ApJS
Schaerer D., de Barros S., 2009, A&A, 502, 423
Schinnerer E., et al., 2016, ApJ, 833, 112
Schmidt M., 1963, ApJ, 137, 758
Schroetter I., Bouché N., Péroux C., Murphy M. T., Contini T., Finley H., 2015, ApJ, 804, 83
Schroetter I., et al., 2016, ApJ, 833, 39
Scoville N., et al., 2016, ApJ, 820, 83
Scoville N., et al., 2017, ApJ, 837, 150
Shen S., Madau P., Guedes J., Mayer L., Prochaska J. X., Wadsley J., 2013, ApJ, 765, 89
Silk J., 1977, ApJ, 211, 638
Smette A., et al., 2015, A&A, 576, A77
Sobral D., Best P. N., Matsuda Y., Smail I., Geach J. E., Cirasuolo M., 2012, MNRAS, 420, 1926
Soto K. T., Lilly S. J., Bacon R., Richard J., Conseil S., 2016a, MNRAS,
Soto K. T., Lilly S. J., Bacon R., Richard J., Conseil S., 2016b, ZAP: Zurich Atmosphere Purge, Astrophysics Source Code Library (ascl:1602.003)
Speagle J. S., Steinhardt C. L., Capak P. L., Silverman J. D., 2014, The Astrophysical Journal Supplement Series, 214, 15
Steidel C. C., 1995, in Meylan G., ed., QSO Absorption Lines. ESO Astrophysics Symposia. Springer-Verlag, Berlin, Germany, p. 139
Steidel C. C., Kollmeier J. A., Shapley A. E., Churchill C. W., Dickinson M., Pettini M., 2002, ApJ, 570, 526
Stewart K. R., Kaufmann T., Bullock J. S., Barton E. J., Maller A. H., Diemand J., Wadsley J., 2011a, ApJ, 735, L1+
Stewart K. R., Kaufmann T., Bullock J. S., Barton E. J., Maller A. H., Diemand J., Wadsley J., 2011b, ApJ, 738, 39
Stewart K. R., Brooks A. M., Bullock J. S., Maller A. H., Diemand J., Wadsley J., Moustakas L. A., 2013, ApJ, 769, 74
Stewart K. R., et al., 2017, ApJ, 843, 47
Storey P. J., Zeippen C. J., 2000, MNRAS, 312, 813
Tacconi L. J., et al., 2010, Nature, 463, 781
Tacconi L. J., et al., 2013, ApJ, 768, 74
Tacconi L. J., et al., 2018, ApJ, 853, 179
Teklu A. F., Remus R.-S., Dolag K., Beck A. M., Burkert A., Schmidt A. S., Schulze F., Steinborn L. K., 2015, ApJ, 812, 29
Turner M. L., Schaye J., Steidel C. C., Rudie G. C., Strom A. L., 2014, MNRAS, 445, 794
Wang J., Koribalski B. S., Serra P., van der Hulst T., Roychowdhury S., Kamphuis P., Chengalur J. N., 2016, MNRAS, 460, 2143
Weilbacher P. M., Streicher O., Urrutia T., Jarno A., Pécontal-Rousset A., Bacon R., Böhm P., 2012, in Society of Photo-Optical Instrumentation Engineers (SPIE) Conference Series. p. 0, doi:10.1117/12.925114
Weilbacher P. M., Streicher O., Urrutia T., Pécontal-Rousset A., Jarno A., Bacon R., 2014, in Manset N., Forshay P., eds, Astronomical Society of the Pacific Conference Series Vol. 485, Astronomical Data Analysis Software and Systems XXIII. p. 451 (arXiv:1507.00034)
Weilbacher P. M., Streicher O., Palsa R., 2016, MUSE-DRP:

MUSE Data Reduction Pipeline, Astrophysics Source Code Library (ascl:1610.004)
Werk J. K., Prochaska J. X., Thom C., Tumlinson J., Tripp T. M., O'Meara J. M., Peeples M. S., 2013, ApJS, 204, 17
Whitaker K. E., et al., 2014, ApJ, 795, 104
White S. D. M., Frenk C. S., 1991, ApJ, 379, 52
Wong T., Blitz L., 2002, ApJ, 569, 157
Zabl J., Freudling W., Møller P., Milvang-Jensen B., Nilsson K. K., Fynbo J. P. U., Le Fèvre O., Tasca L. A. M., 2016, A&A, 590, A66
Zhu G., Ménard B., 2013, ApJ, 770, 130
van de Voort F., Schaye J., 2012, MNRAS, 423, 2991
van de Voort F., Schaye J., Booth C. M., Haas M. R., Dalla Vecchia C., 2011, MNRAS, 414, 2458
van den Bergh S., 1962, AJ, 67, 486
van der Walt S., Colbert S. C., Varoquaux G., 2011, Computing in Science Engineering, 13, 22
van der Wel A., et al., 2012, ApJS, 203, 24

APPENDIX A: UNCERTAINTIES OF INCLINATION AND AZIMUTHAL ANGLE ESTIMATES

In this appendix, we review the uncertainties (statistical and systematics) on the three key parameters necessary for this paper, namely the galaxies' inclinations, i, position angles, α (or PA), and maximum rotation velocities, $v_{\rm max}$.

The statistical error estimates obtained from $GalPak^{3D}$ are the Bayesian uncertainties under the assumption of the model. From a comparison with the dispersion of the differences between input and measured values in a matched sample of simulated galaxies taken from Bouché et al. (2015) ($GalPak^{3D}$ reference paper), we inferred that the statistical uncertainties stated by $GalPak^{3D}$ are mainly accurate, but potentially underestimated by about 20%. Therefore, we conservatively increased the Bayesian uncertainties by 20%.

The systematic errors can be caused by mismatches between the parameterised model and the data (especially at high SNR) and/or a slightly imperfect characterisation of the PSF. We have estimated the level of systematic error for the morphological parameters (PA and i) in two different ways. First, we compare two independent methods ($GalPak^{3D}$ and *GALFIT*) on our seeing limited data, and second, we compare the seeing-limited $GalPak^{3D}$ morphological parameters on a separate sample with ancillary *HST* morphology.

The first method compares the $GalPak^{3D}$ (see §5.1.1) and the *GALFIT* (2D) (see §5.2) morphological measurements (PA, i) for our sample galaxies. We also used two different measurements of the PSF parameters, as described in §3.1.2, namely the *MPDAF* based estimates of the Moffat profile for the $GalPak^{3D}$ measurements, and the *Pampelmuse* based estimates of the PSF for the *GALFIT* measurements. Thus, by comparing measurements from the two estimates we capture uncertainties all due to the fitting code, the way we extract the PSF, and differences due to using continuum light and line emission.

The result of this comparison is shown both for i and PA in Fig. A1. In general, the agreement between the two estimates is good, importantly without any strong outliers. The rms difference between the *GALFIT* and $GalPak^{3D}$ is $\sim$ 9 deg for both i and PA. Assuming that the *GALFIT* and $GalPak^{3D}$ measurements contribute about equally, we attribute a 7 deg systematic uncertainty to the $GalPak^{3D}$ measurements (for α and i). Note this is always larger than the $GalPak^{3D}$ statistical uncertainties, and thus can be safely used to cover both statistical and systematic uncertainties.

For the second method, we compared the morphological parameters (i in particular) obtained with $GalPak^{3D}$ for a larger sample of about 60 [O II] emitters (Bouché et al. in prep.) in seeing-limited MUSE observations in the UDF (Bacon et al. 2017) againt the i measurements from the *HST* H-band from van der Wel et al. (2012). This second method gives a scatter of about 7 deg between the two estimates, confirming our error budget estimate.

We end this section with a quantitative assessment of the systematic uncertainties for the $v_{\rm max}$ parameter. Using the same UDF [O II] emitter sample, we compared $v_{\rm max}$ measurements from $GalPak^{3D}$ measurements to $v_{\rm max}$ determined with the *CAMEL* code (Epinat et al. 2012) discussed in Contini et al. (in prep.) and found a relative systematic error of about 10%. Thus, to the $v_{\rm max}$ error budget stated in Table 4 of the main manuscript, we added this 10% relative error to the statistical errors in quadrature.

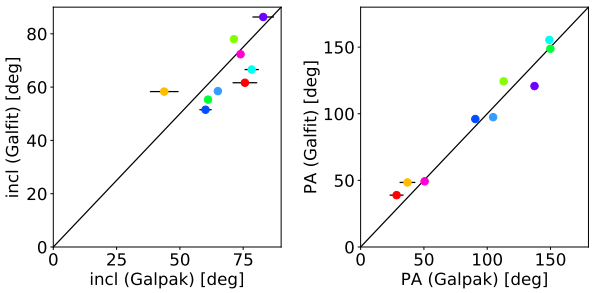

Figure A1. Comparison between $GalPak^{3D}$ and *GALFIT* based estimates for the inclination, i, (left) and position angle, PA, (right) for each of the 9 galaxies in our sample. The statistical errors obtained from $GalPak^{3D}$ are shown as error bars, and are in some cases not visible, as they are smaller than the marker size.

APPENDIX B: FIELD, SPECTRAL, AND KINEMATIC PLOTS FOR EACH OF THE ABSORBERS

The same information as available in Fig. 4 and Fig. 5 for *J0145*, meaning an [O II] NB FoV image around the absorber redshift, kinematics of the primary galaxies, and the spectral SED, is shown in Fig. B1 to B8 for the eight other galaxy-absorber pairs of our sample.

APPENDIX C: SUPPLEMENTARY TABLES

APPENDIX D: SUPPLEMENTARY FIGURES

This paper has been typeset from a TEX/LATEX file prepared by the author.

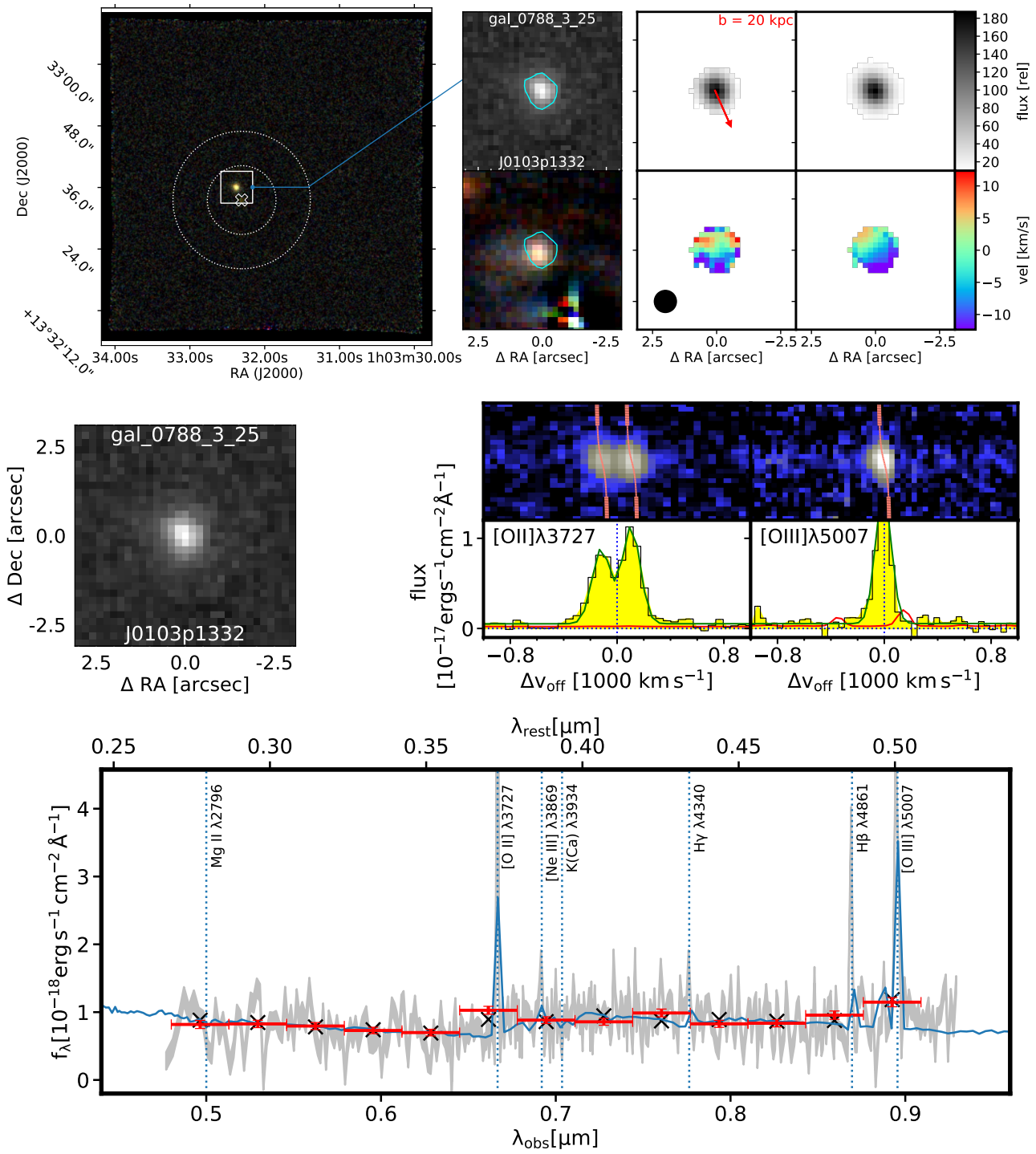

Figure B1. Same as in Figs. 4 and 5, but here for the main galaxy associated to the absorber abs_J0103p1332_0788.

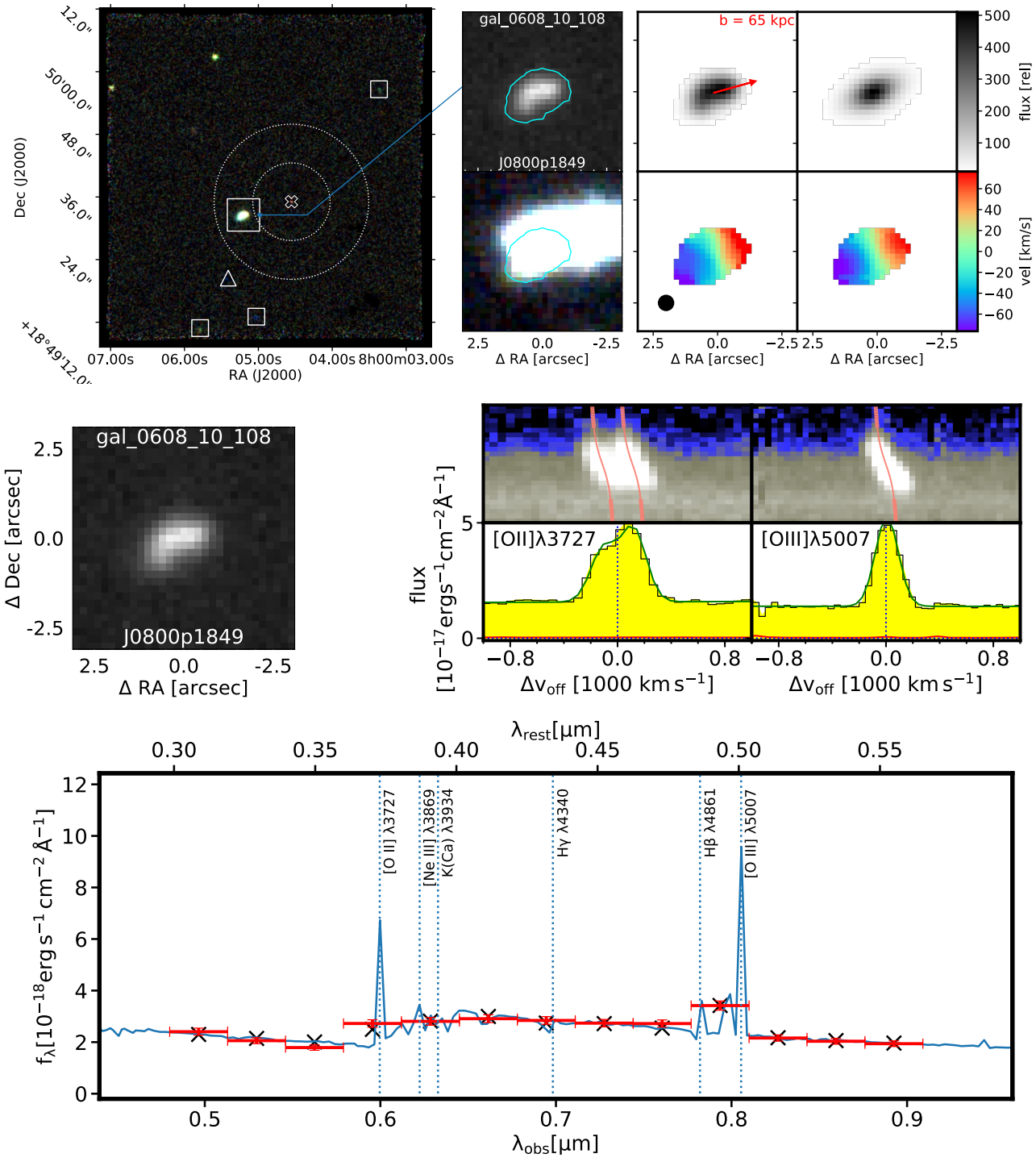

Figure B2. Same as in Figs. 4 and 5, but here for the main galaxy associated with the absorber abs_J0800p1849_0608. A pure absorption line galaxy is indicated as a white triangle. Here the grey line (aperture spectrum) is not visible, as the contamination from an unrelated foreground source is large.

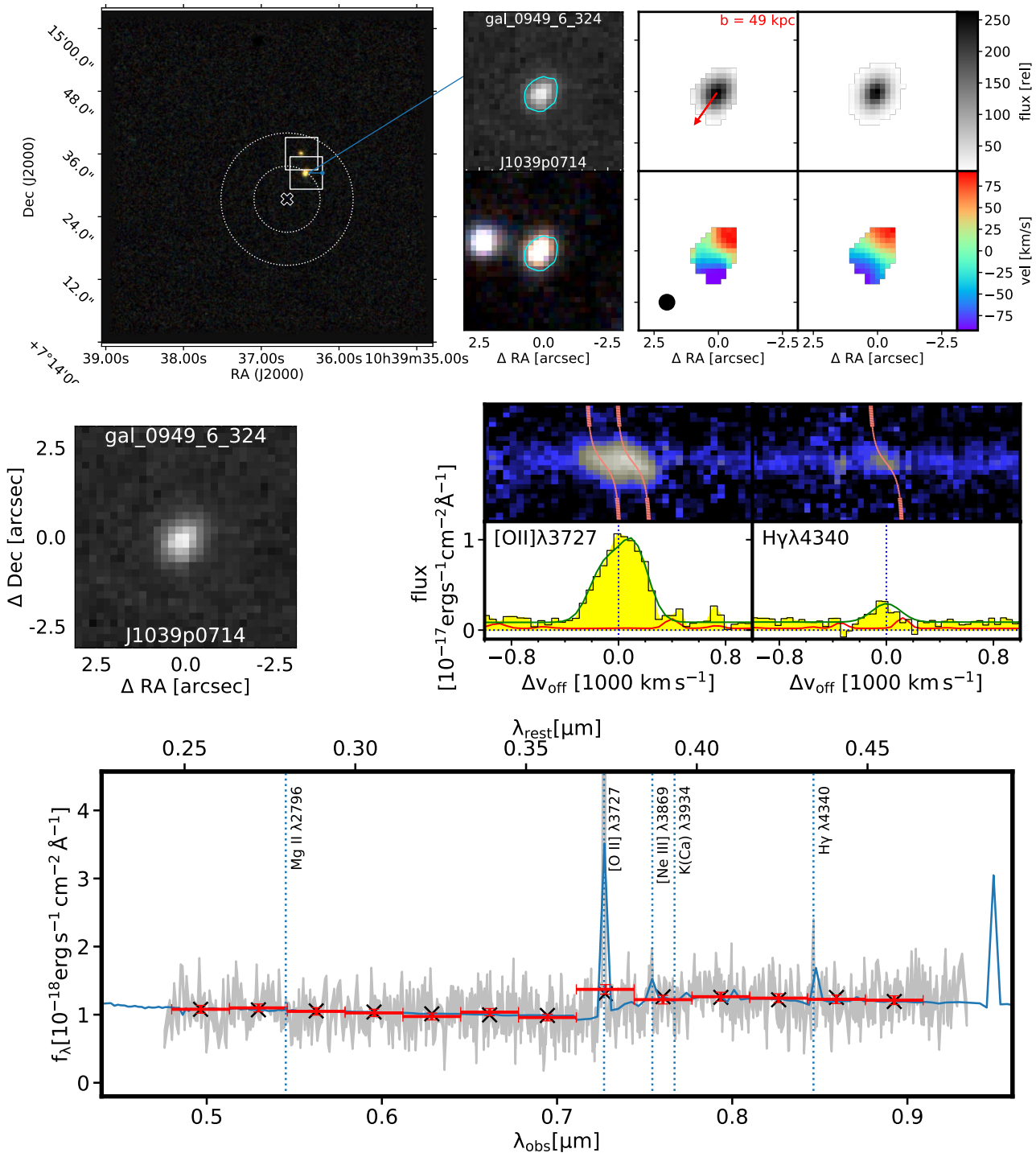

Figure B3. Same as in Figs. 4 and 5, but here for the main galaxy associated with the absorber abs_J1039p0714_0949.

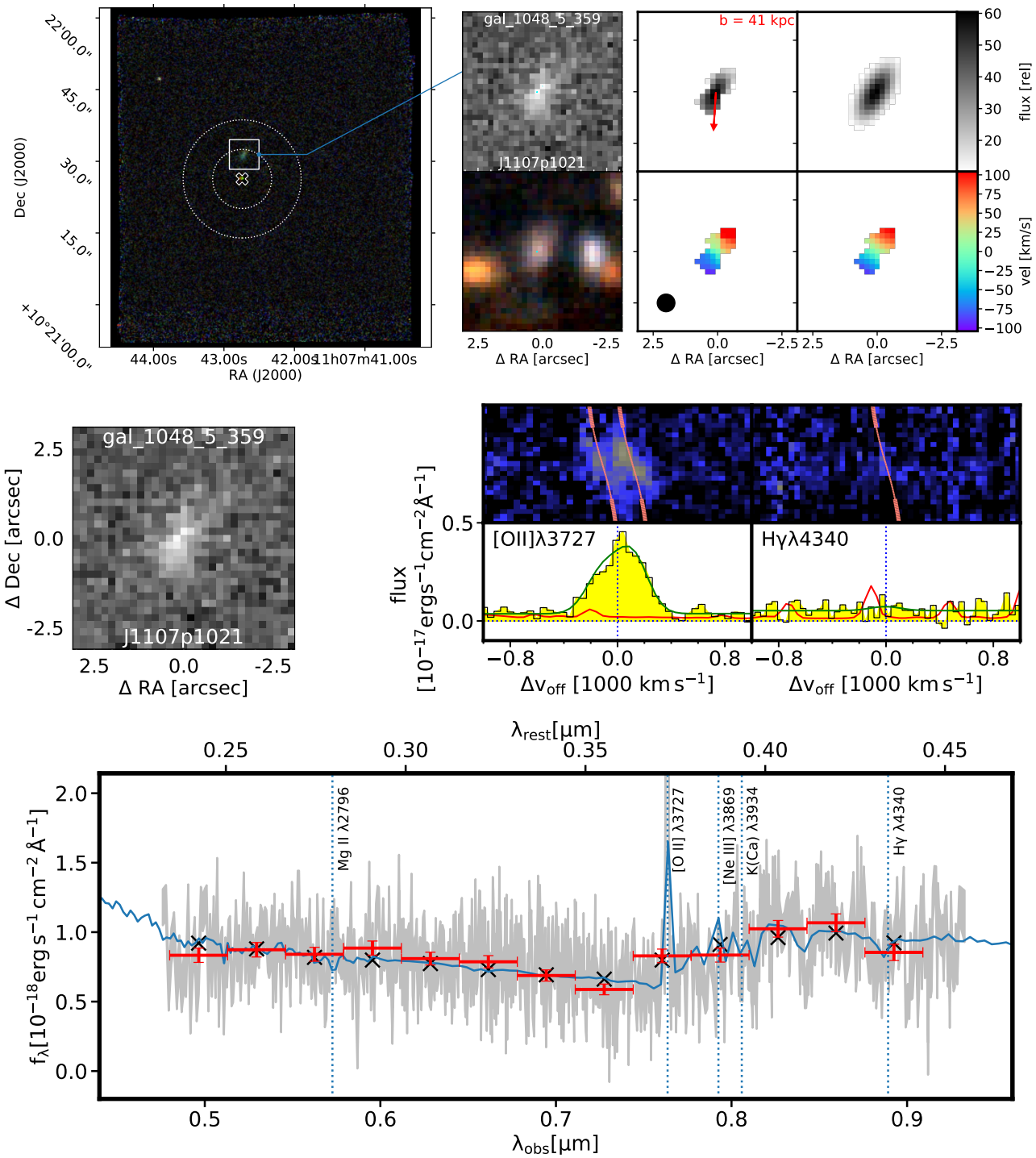

Figure B4. Same as in Figs. 4 and 5, but here for the main galaxy associated with the absorber abs_J1107p1021_1048.

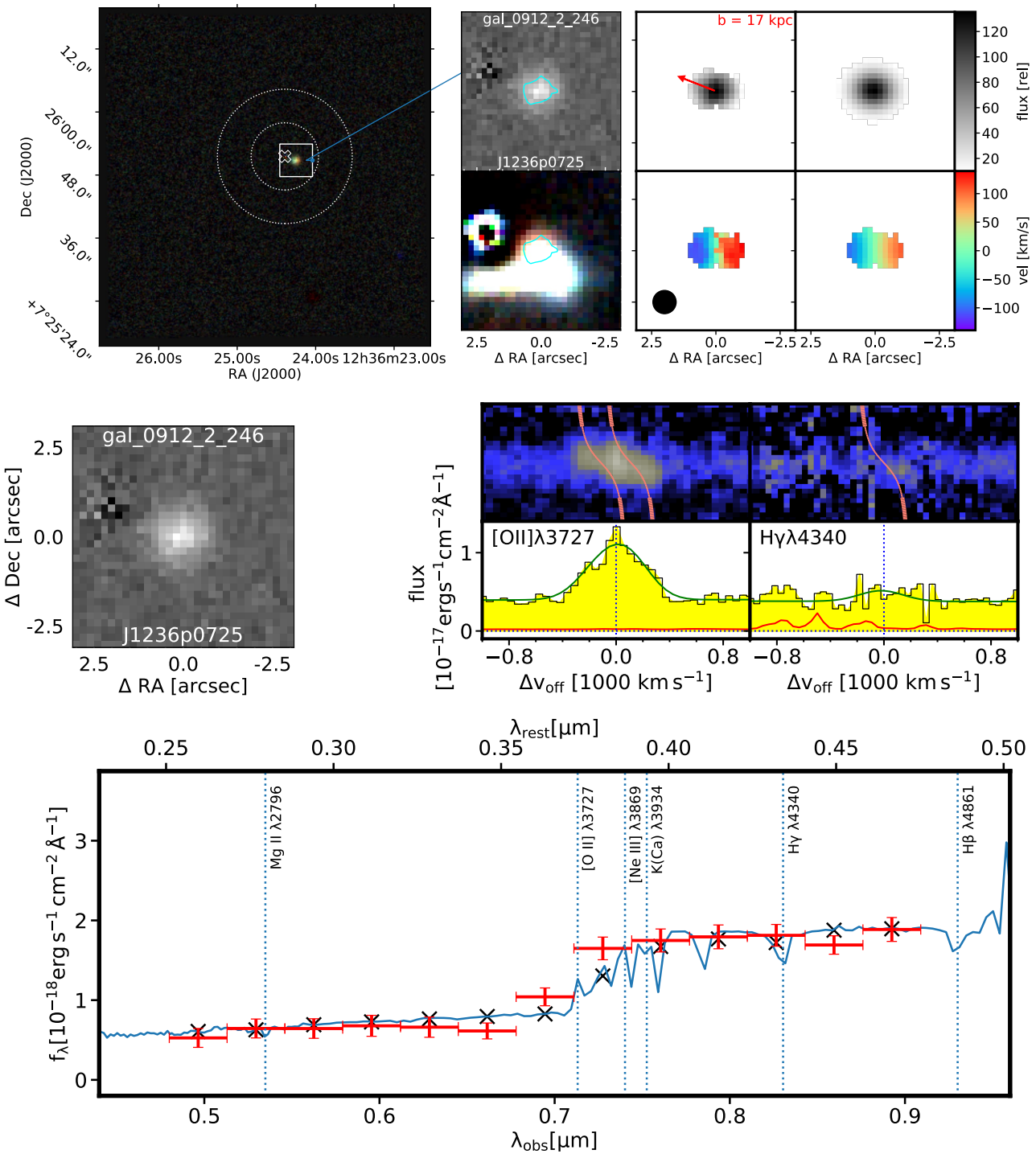

Figure B5. Same as in Figs. 4 and 5, but here for the main galaxy associated with the absorber abs_J1236p0725_0912. Here the grey line (aperture spectrum) is not visible, as the contamination from an unrelated foreground source is large.

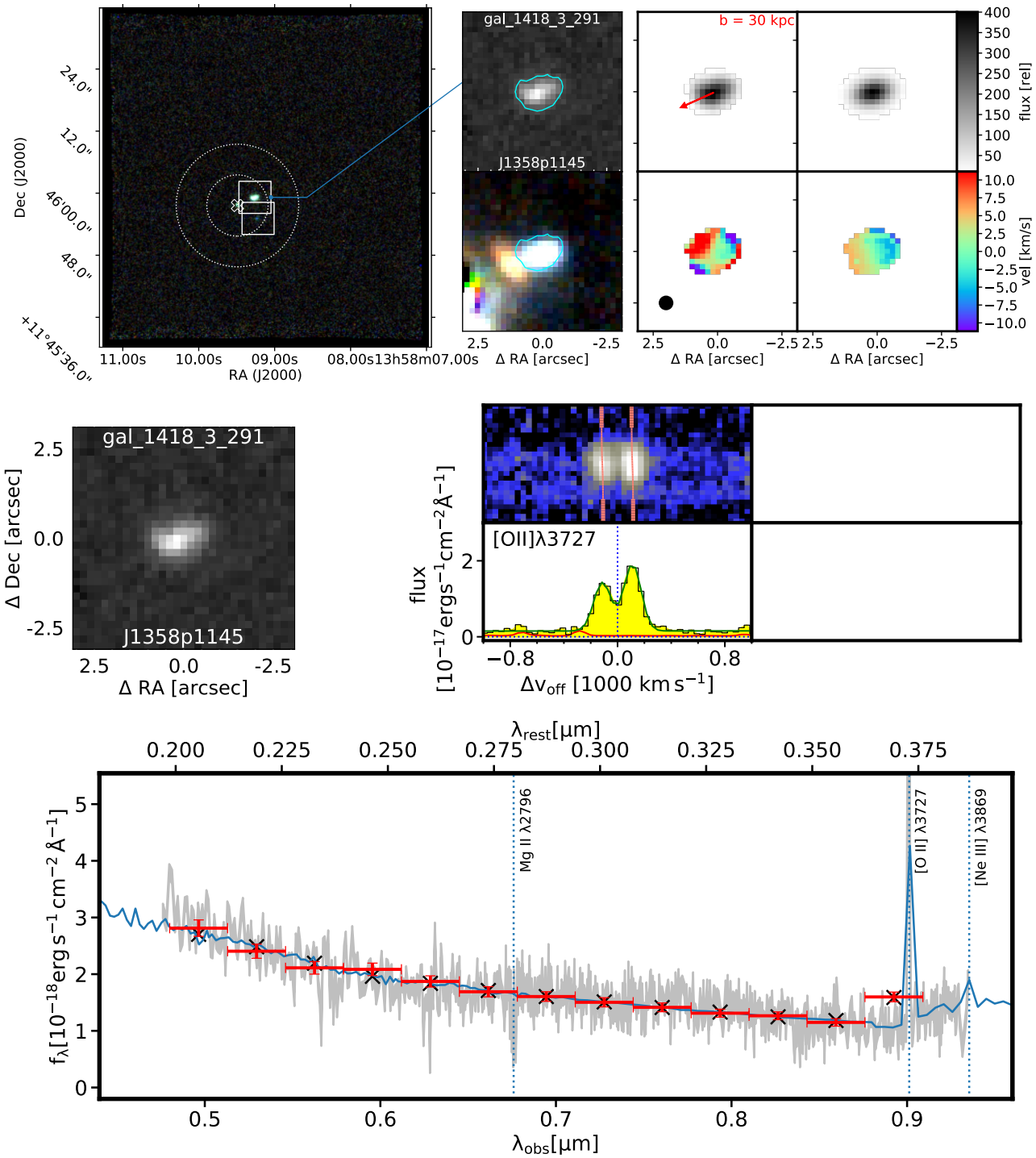

Figure B6. Same as in Figs. 4 and 5, but here for the main galaxy associated with the absorber abs_J1358p1145_1418.

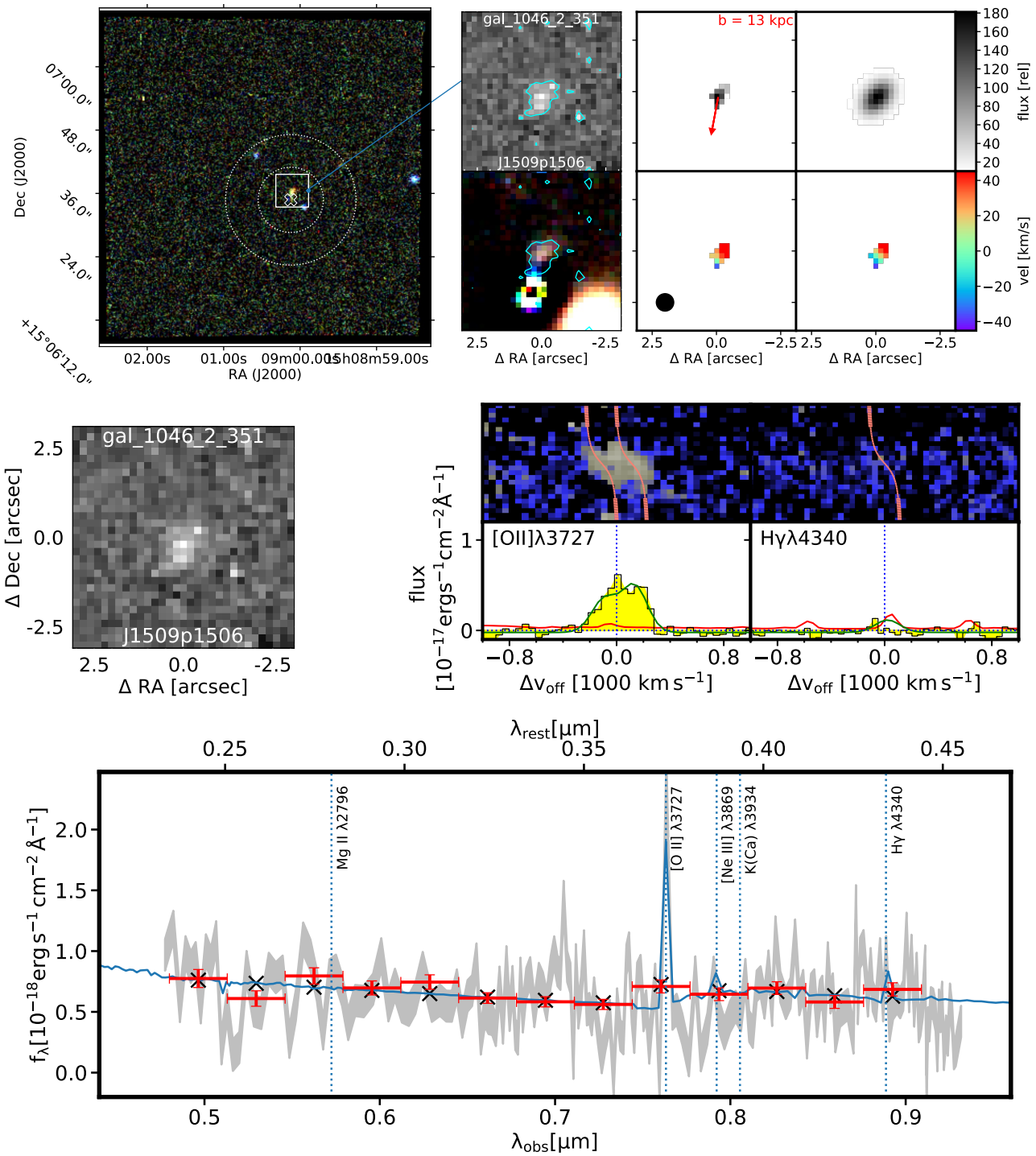

Figure B7. Same as in Figs. 4 and 5, but here for the main galaxy associated with the absorber abs_J1509p1506_1046.

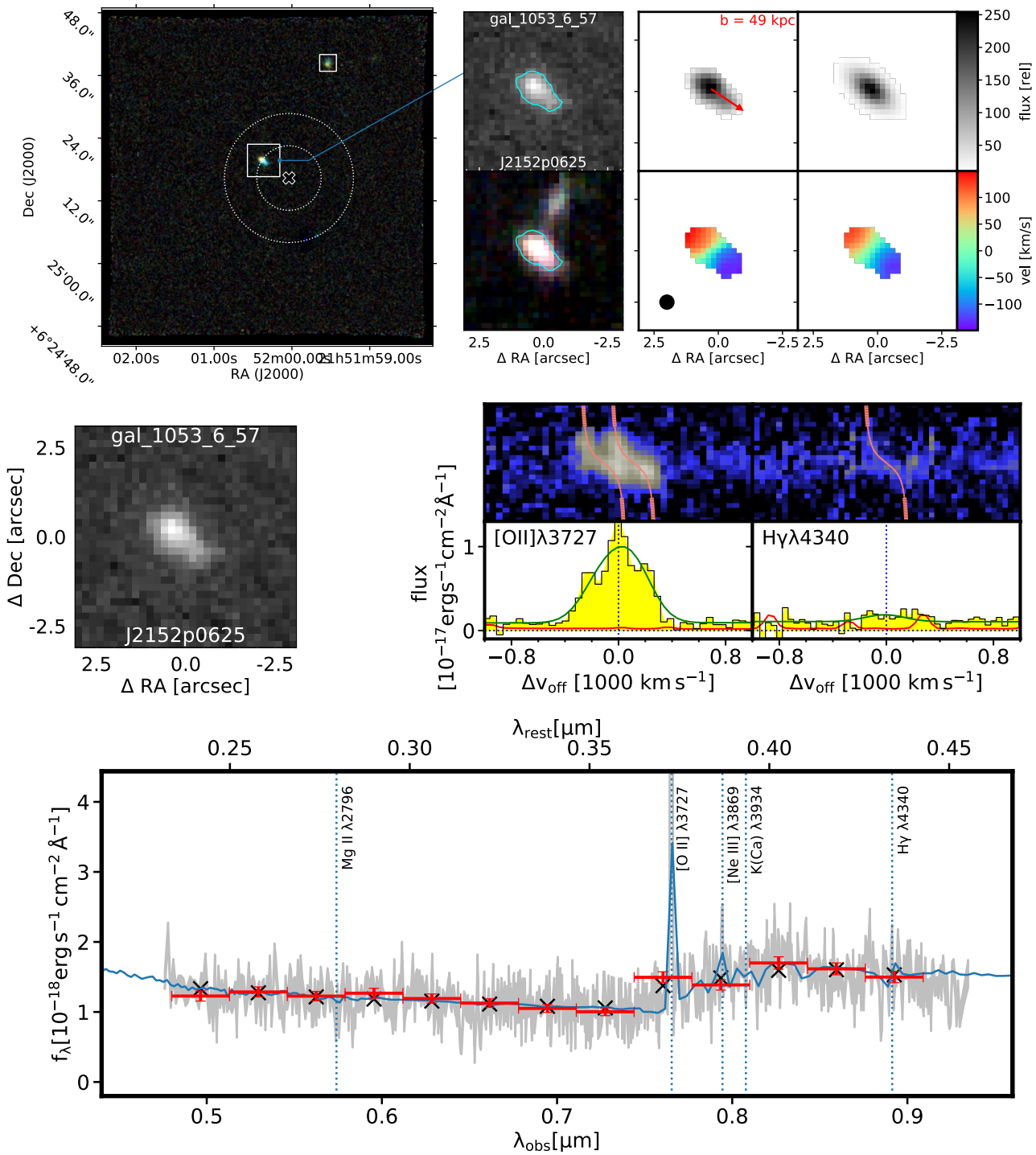

Figure B8. Same as in Figs. 4 and 5, but here for the main galaxy associated with the absorber abs_J2152p0625_1053.

MUSE Observations

Quasar	R.A.	Dec.	T_{exp}	Seeing (G.)	Seeing (M.)	Date-Obs	Prog. IDs	Refs
(1)	(2)	(3)	(4)	(5)	(6)	(7)	(8)	(9)
J0014m0028	00:14:53.4	-00:28:28	6.3	0.97	0.78	2015-08-23, 2015-09-10, 2015-10-12	095.A-0365(A), 096.A-0164(A)	This work
J0014p0912	00:14:53.2	+09:12:18	10.8	1.06	0.85	2014-10-19, 2014-10-20, 2014-10-24	094.A-0211(B)	This work
J0015m0751	00:15:35.2	-07:51:03	9.0	0.98	0.80	2015-10-09, 2015-10-10, 2016-08-31	096.A-0164(A), 097.A-0138(A)	This work
J0058p0111	00:58:55.8	+01:11:29	7.2	0.97	0.77	2015-11-08, 2016-08-29	096.A-0164(A), 097.A-0138(A)	This work
J0103p1332	01:03:32.3	+13:32:34	7.2	1.05	0.84	2015-11-11, 2015-11-12	096.A-0164(A)	This work
J0131p1303	01:31:36.4	+13:03:31	7.2	1.04	0.81	2014-10-27	094.A-0211(B)	This work
J0134p0051	01:34:05.8	+00:51:09	10.2	0.94	0.73	2015-10-14, 2015-10-15, 2016-08-31	096.A-0164(A), 097.A-0138(A)	This work
J0145p1056	01:45:13.1	+10:56:27	6.0	1.03	0.85	2015-11-12, 2016-08-29	096.A-0164(A), 097.A-0138(A)	This work
J0800p1849	08:00:04.6	+18:49:35	7.2	0.73	0.56	2014-12-24	094.A-0211(B)	This work
J0838p0257	08:38:52.1	+02:57:04	12.0	0.73	0.54	2016-02-01, 2016-02-02, 2017-02-02	096.A-0164(A), 098.A-0216(A)	This work
J0937p0656	09:37:49.6	+06:56:56	7.2	0.83	0.67	2015-04-15, 2015-04-17	095.A-0365(A)	This work
J1039p0714	10:39:36.7	+07:14:27	12.0	0.78	0.61	2016-04-07, 2016-04-08, 2017-01-27	097.A-0138(A), 098.A-0216(A)	This work
J1107p1021	11:07:42.7	+10:21:26	12.0	0.92	0.70	2016-03-11, 2017-01-28, 2017-02-01	096.A-0164(A), 098.A-0216(A)	This work
J1107p1757	11:07:35.3	+17:57:31	7.2	1.05	0.88	2015-04-22, 2015-04-23	095.A-0365(A)	This work
J1236p0725	12:36:24.4	+07:25:52	6.0	1.13	0.91	2016-03-12	096.A-0164(A)	This work
J1314p0657	13:14:05.6	+06:57:22	6.0	0.68	0.53	2016-04-06, 2016-04-07	097.A-0138(A)	This work
J1352p0614	13:52:17.7	+06:14:33	6.0	1.22	0.98	2017-04-22, 2017-04-23	099.A-0059(A)	This work
J1358p1145	13:58:09.5	+11:45:58	6.0	0.72	0.54	2016-04-09	097.A-0138(A)	This work
J1425p1209	14:25:38.1	+12:09:19	3.6	1.19	0.96	2016-05-11	097.A-0138(A)	This work
J1509p1506	15:09:00.1	+15:06:35	3.0	0.85	0.70	2017-04-22	099.A-0059(A)	This work
J2137p0012	21:37:48.4	+00:12:20	3.6	0.94	0.74	2014-09-23	094.A-0211(B)	paper I
J2152p0625	21:52:00.0	+06:25:16	7.2	0.74	0.58	2014-09-24	094.A-0211(B)	paper I

Table C1. Details of MUSE observations for the 22 MEGAFLOW fields as used in this study. (1) Quasar/Field identifier; (2) Right ascension of the QSO [hh:mm:ss; J2000]; (3) Declination of the QSO [dd:mm:ss; J2000]; (4) Total MUSE exposure time [ks]; (5) Seeing FWHM measured at 7050Å by fitting a Gaussian [arcsec]; (6) Seeing FWHM measured at 7050Å by fitting a Moffat profile with $\beta = 2.5$ [arcsec]; (7) Date of Observations; (8) ESO Program IDs; (9) Reference.

UVES Observations

Quasar	R.A.	Dec.	z_{em}	T_{exp}	Seeing	Date-Obs	Setting	Prog. IDs	Refs
(1)	(2)	(3)	(4)	(5)	(6)	(7)	(8)	(9)	(10)
J0014m0028	00:14:53.4	-00:28:28	1.92	9015	0.8	2015-10-03	390 & 564	096.A-0609(A)	This work
J0014p0912	00:14:53.2	+09:12:18	2.34	6010, 1483	0.8, 0.5	2015-11-09, 2016-10-28	437 & 760, 390 & 564	096.A-0609(A), 098.A-0310(A)	This work
J0015m0751	00:15:35.2	-07:51:03	0.87	12020	0.7	2016-10-29, 2016-12-27, 2016-12-28	390 & 564	098.A-0310(A)	This work
J0058p0111	00:58:55.8	+01:11:29	1.22	1483, 1483	0.9, –[a]	2016-12-29, 2016-12-30	437 & 760, 390 & 564	098.A-0310(A)	This work
J0103p1332	01:03:32.3	+13:32:34	1.66	9015	0.6	2016-10-28, 2016-10-29, 2016-11-01	390 & 564	098.A-0310(A)	This work
J0131p1303	01:31:36.4	+13:03:31	1.59	6010	1.0	2015-10-14	390 & 580	096.A-0609(A)	This work
J0134p0051	01:34:05.8	+00:51:09	1.52	5710, 1483	0.6, 0.4	2016-10-29, 2016-12-03	437 & 760, 390 & 580	098.A-0310(A)	This work
J0145p1056	01:45:13.1	+10:56:27	0.94	12020	0.6	2015-11-11, 2016-09-03, 2016-10-28	390 & 564	096.A-0609(A), 097.A-0144(A), 098.A-0310(A)	This work
J0800p1849	08:00:04.6	+18:49:35	1.29	6010	0.9	2015-12-10	520	096.A-0609(A)	This work
J0838p0257	08:38:52.1	+02:57:04	1.77	1483, 1483	0.6, 1.0	2015-11-20, 2016-12-22	390 & 564, 600	096.A-0609(A), 098.A-0310(A)	This work
J0937p0656	09:37:49.6	+06:56:56	1.82	9015	0.7	2015-12-20, 2016-01-11, 2016-03-07	390 & 564	096.A-0609(A)	This work
J1039p0714	10:39:36.7	+07:14:27	1.53	9015	0.8	2016-04-03	346 & 580	097.A-0144(A)	This work
J1107p1021	11:07:42.7	+10:21:26	1.92	6010	1.0	2016-02-09, 2016-03-07	390 & 580	096.A-0609(A)	This work
J1107p1757	11:07:35.3	+17:57:31	2.15	9015	1.0	2016-01-11, 2016-03-06, 2016-03-07	437 & 760	096.A-0609(A)	This work
J1236p0725	12:36:24.4	+07:25:52	1.61	6010, 1483	0.4, 0.9	2016-03-06, 2016-04-06	437 & 760, 600	096.A-0609(A), 097.A-0144(A)	This work
J1314p0657	13:14:05.6	+06:57:22	1.88	1483	0.4	2016-04-06	390 & 564	097.A-0144(A)	This work
J1352p0614	13:52:17.7	+06:14:33	1.80	1483	0.7	2016-05-31	437 & 760	097.A-0144(A)	This work
J1358p1145	13:58:09.5	+11:45:58	1.48	1483, 1483	0.5, 0.5	2016-04-06	346 & 860, 390 & 564	097.A-0144(A)	This work
J1425p1209	14:25:38.1	+12:09:19	1.62	1483, 1483	0.6, 0.5	2016-04-06, 2016-05-31	390 & 564, 520	097.A-0144(A)	This work
J1509p1506	15:09:00.1	+15:06:35	2.24	6010	0.6	2016-04-03, 2016-04-06	600	097.A-0144(A)	This work
J2137p0012	21:37:48.4	+00:12:20	1.67	4487	1.0	2014-10-18	390 & 564	293.A-5038(A)	Paper I
J2152p0625	21:52:00.0	+06:25:16	2.38	9015	1.2	2014-10-20, 2014-10-23, 2014-11-17	390 & 580	293.A-5038(A)	Paper 1

Table C2. Details of UVES observations for the 22 MEGAFLOW Quasars. (1) Quasar identifier; (2) Right ascension of QSO [hh:mm:ss; J2000]; (3) Declination of QSO [dd:mm:ss; J2000]; (4) Emission redshift of the QSO; (5) Total UVES exposure time split into settings [s]; (6) Seeing FWHM measured by DIMM split into settings [arcsec] ; (7) Date of Observations; (8) UVES settings (Central wavelengths of gratings in [nm]); (9) ESO Program IDs; Comments: a) For part of the observations DIMM measurements unavailable.

	Gal ID	z	Δv **I**	Δv **II**	Δv **III**
	(1)	(2)	(3)	(4)	(5)
	J0103	0.7882	5	-5	-7
	J0145	0.5500	40	53	7
	J0800	0.6082	11	26	7
	J1039	0.9494	14		0
	J1107	1.0481	-7		-5
	J1236	0.9128	14		-21
	J1358	1.4171	2		-1
	J1509	1.0469	-7		22
	J2152	1.0530	-19		-12

Table C3. Comparison of different redshift measurements: (2): z is the redshift obtained with $GalPak^{3D}$ on the [O II] doublet. (3) Δv **I** is the velocity difference between the redshift obtained by visual inspection of the [O II] PVD and z. (4) Δv **II** is the same as for Δv **I**, but here based on [O III] λ5007. MUSE covers [O III] only for the three lowest redshift galaxies. (5) Δv **III** is the velocity difference between the redshift obtained by the 1D line fit and the $GalPak^{3D}$ redshift (z). (3–5) are in km s^{-1}.

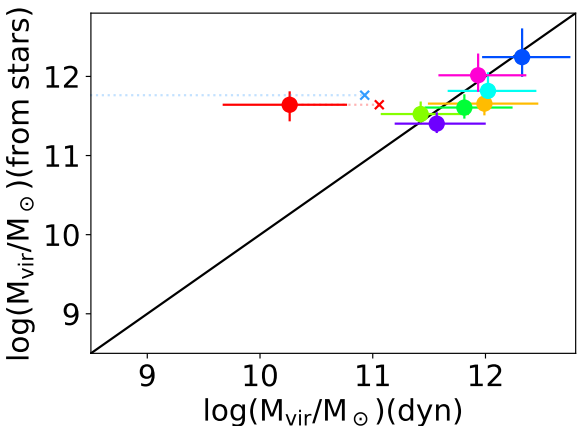

Figure D1. Comparison between halo mass estimates ($M_{\rm vir}$) from two different methods plotted against each other. $M_{\rm vir}$(from stars) was obtained from the stellar mass - halo mass relationship, while $M_{\rm vir}(dyn)$ was determined based on the dynamics of the galaxies. For two of the galaxies, *J0103* (red) and *J1358* (light blue), the latter is plotted based on two different estimates of the virial velocity, once taking account for the pressure support in the galaxy dynamics (little cross) and once not taking this into account (full circle; for *J1358* the circle is outside of the plotted range.).

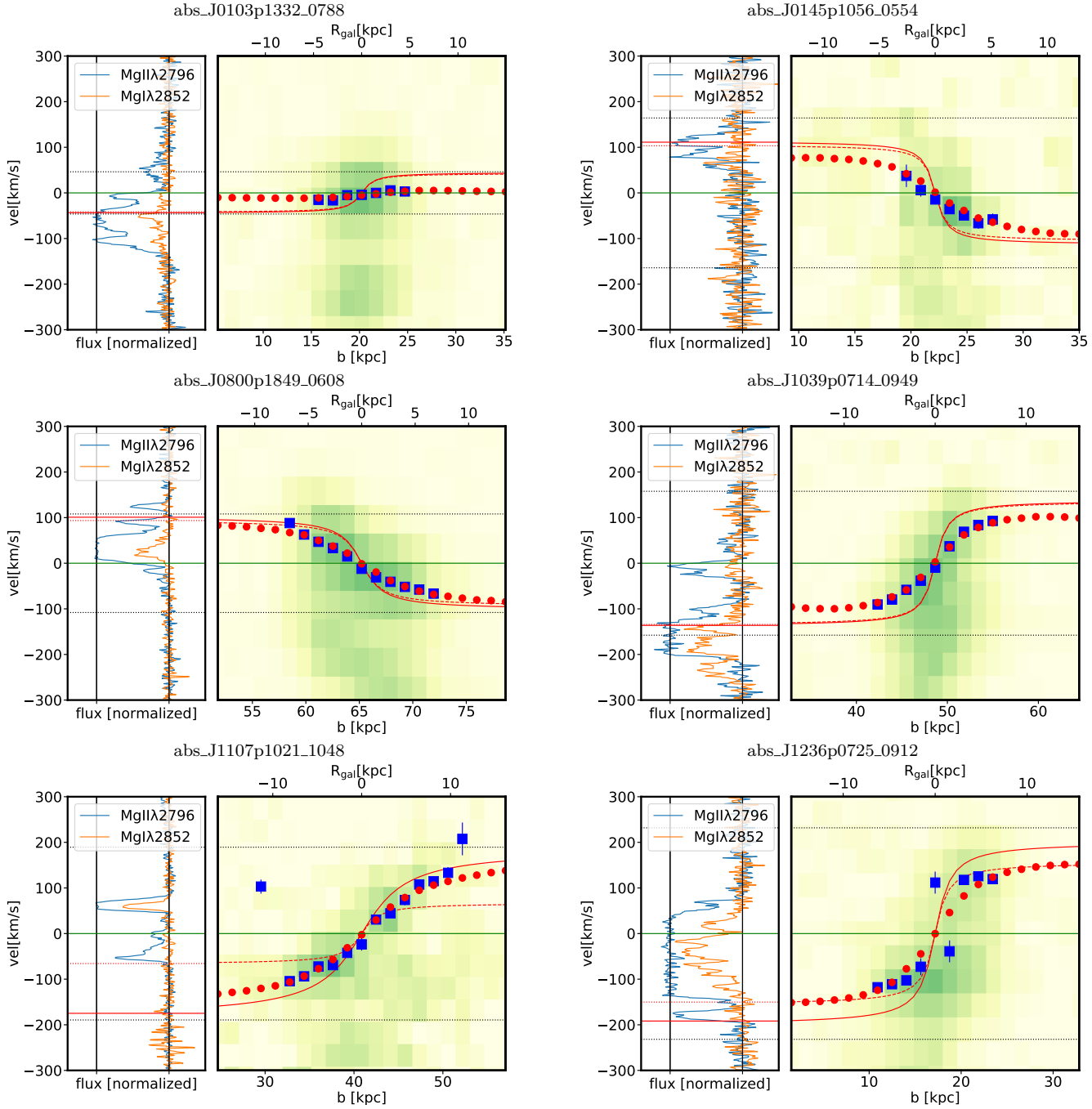

Figure D2. Comparison of galaxy and absorber kinematics for each of the nine galaxy-absorber pairs. The **right panel** shows the 1D galaxy rotation curve (blue points) obtained from the 2D PVD diagram (shown as background image) on the [O II] doublet (see §6.1). Among the blue points are a few obvious outliers where the automatic doublet fitting algorithm failed. The red points are obtained by reproducing this measurement procedure on the seeing convolved best-fit *GalPak*^{3D} model. The solid red line represents the intrinsic *GalPak*^{3D} rotation curve along the galaxy major-axis. The dashed red line represents the modeled rotation curve along the line connecting the galaxy and quasar positions on the sky. The lower x-axis represents the distance b from the quasar along this connecting line. The upper x-axis shows the galacto-centric distance along the galaxy's major axis. In the **left panel** the Mg II λ2796 and Mg I λ2852 absorption profiles are shown on the same velocity scale as the galaxy rotation curve. The solid red line in this panel indicates $V_{\rm max}$ at the observed inclination, which is a continuation of the red curve in the right panel. Similarly, the red dashed line is the continuation of the rotation curve along the galaxy-quasar axis. Further, the black dotted line shows $v_{\rm max}$ at $incl = 90°$ and the green line is the systemic redshift as obtained from *GalPak*^{3D} ($v = 0\,{\rm km\ s^{-1}}$).

ID	ϕ	R	$R/r_{\rm vir}$	$v_\phi/v_{\rm vir}$ (no infall)	$v_\phi/v_{\rm vir}$ (infall same)	$v_\phi/v_{\rm vir}$ (infall opposite)	$\log_{10}(\cos(i)N_{\rm HI})$	$\dot{M}_{\rm in}(R)$
(1)	(2)	(3)	(4)	(5)	(6)	(7)	(8)	(9)
J0103	17^{+30}_{-11}	21^{+8}_{-1}	$0.16^{+0.10}_{-0.03}$	$0.46^{+0.24}_{-0.04}$	$0.27^{+0.13}_{-0.27}$	$0.65^{+0.68}_{-0.12}$	18.9 ± 0.5	$0.9^{+2.0}_{-0.6}$
J0145	22 ± 9	23 ± 1	$0.12^{+0.06}_{-0.04}$	$1.17^{+0.65}_{-0.35}$	$0.93^{+0.65}_{-0.36}$	$1.41^{+0.69}_{-0.36}$	18.6 ± 0.5	$0.7^{+1.5}_{-0.5}$
J0800	22^{+21}_{-14}	70^{+17}_{-4}	$0.59^{+0.37}_{-0.19}$	$0.27^{+0.14}_{-0.06}$	$0.03^{+0.17}_{-0.03}$	$0.51^{+0.42}_{-0.18}$	18.7 ± 0.5	$1.8^{+4.0}_{-1.3}$
J1039	10^{+15}_{-7}	49^{+3}_{-1}	$0.36^{+0.14}_{-0.10}$	$1.16^{+0.46}_{-0.29}$	$1.05^{+0.40}_{-0.34}$	$1.27^{+0.55}_{-0.27}$	18.9 ± 0.5	$2.7^{+6.0}_{-2.0}$
J1107	69^{+12}_{-13}	100^{+123}_{-34}	$0.66^{+1.27}_{-0.35}$	$-0.98^{+0.39}_{-1.40}$	–	$0.56^{+0.98}_{-0.46}$	17.9 ± 0.5	$0.7^{+1.8}_{-0.6}$
J1236	39^{+12}_{-11}	20^{+3}_{-2}	$0.10^{+0.05}_{-0.03}$	$0.29^{+0.13}_{-0.08}$	–	$0.77^{+0.34}_{-0.20}$	19.8 ± 0.5	$12.5^{+27.5}_{-9.1}$
J1358	22^{+16}_{-14}	32^{+4}_{-2}	$0.30^{+0.09}_{-0.06}$	$0.48^{+0.13}_{-0.07}$	$0.24^{+0.15}_{-0.16}$	$0.72^{+0.32}_{-0.18}$	19.9 ± 0.5	$17.7^{+38.4}_{-12.3}$
J1509	79^{+7}_{-11}	56^{+109}_{-27}	$0.52^{+1.52}_{-0.33}$	$4.97^{+10.97}_{-2.58}$	$1.92^{+4.48}_{-1.40}$	$8.02^{+17.39}_{-4.08}$	18.8 ± 0.5	$2.2^{+6.5}_{-1.9}$
J2152	19^{+26}_{-12}	52^{+16}_{-2}	$0.36^{+0.26}_{-0.11}$	$-0.43^{+0.10}_{-0.26}$	–	$0.00^{+0.06}_{-0.00}$	18.4 ± 0.5	$1.0^{+2.1}_{-0.7}$

Table C4. Geometrical and kinematical constraints for the absorbing gas inferred under the assumption of an extended gas disk. (2) Position angle of quasar sight-line in disk plane as defined in Eq. (4) [deg]; (3) Galacto-centric radius of quasar sight-line as defined in Eq. (5) [kpc]; (4) R normalised by $r_{\rm vir}$; (5) Tangential velocity (normalised by $v_{\rm vir}$) as shown in Fig. 9 estimated under the assumption of $v_{\rm r}=0$ (see Eq. (8)); (6 & 7) Tangential velocity (normalised by $v_{\rm vir}$) as shown in Fig. 10 estimated under the assumption of $v_{\rm r}=-0.6v_{\rm vir}$ (see Eq. (11)). Depending on the disk's unknown sign of inclination the signs of the projected components of v_ϕ and $v_{\rm r}$ can be the same or the opposite, leading to the two solutions 6) and 7) for v_ϕ, respectively. Due to the requirement of co-rotation with the galaxy disk, it is possible that no solution can be found (indicated by "–"). Error intervals that are consistent with zero indicate that only part of the uncertainty interval is consistent with co-rotation; (8) HI column density perpendicular to disk (based on MgII equivalent width) [cm^{-2}]; (9) Mass accretion rate [$M_\odot$ yr^{-1}].

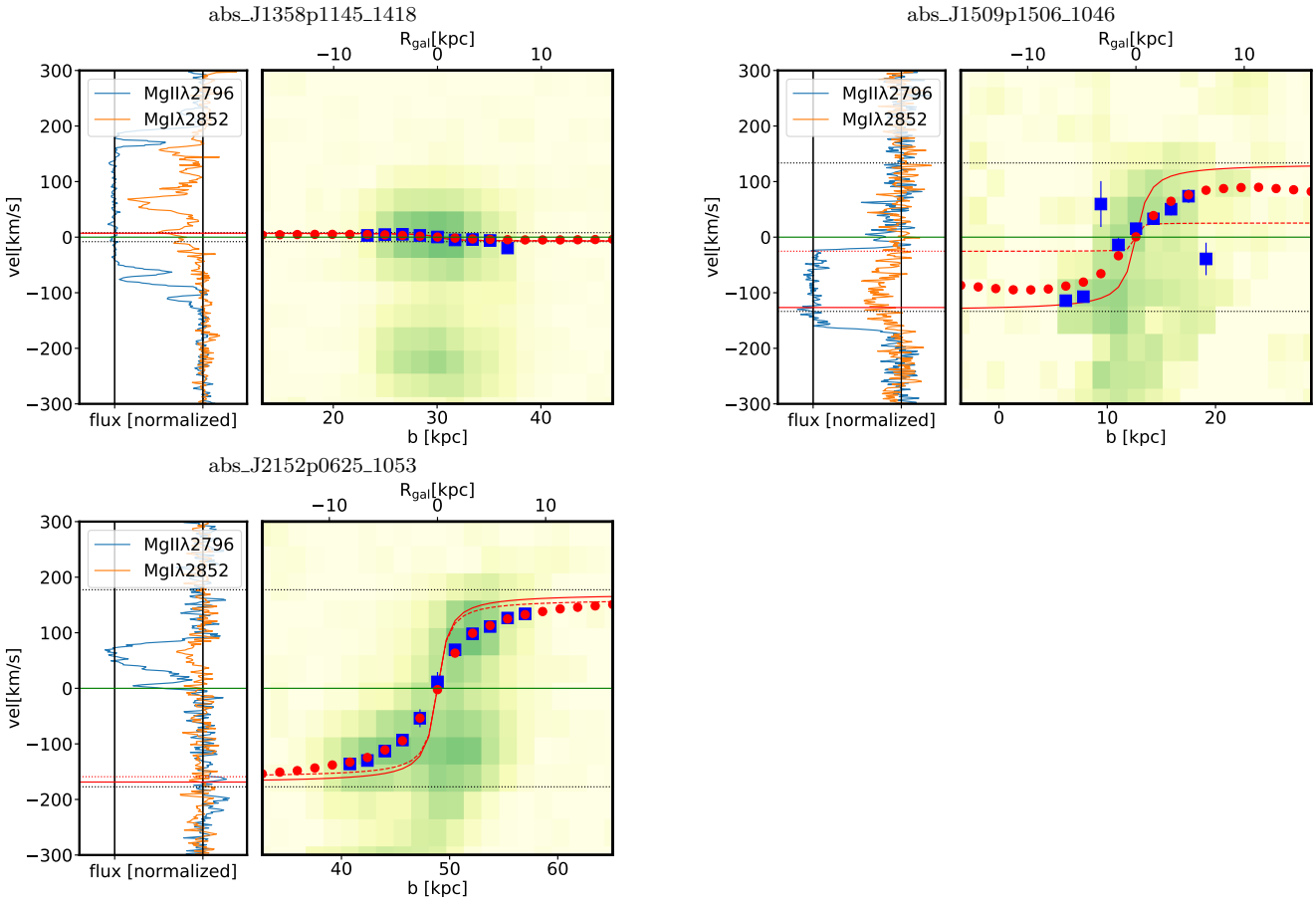

Figure D2 – *continued*

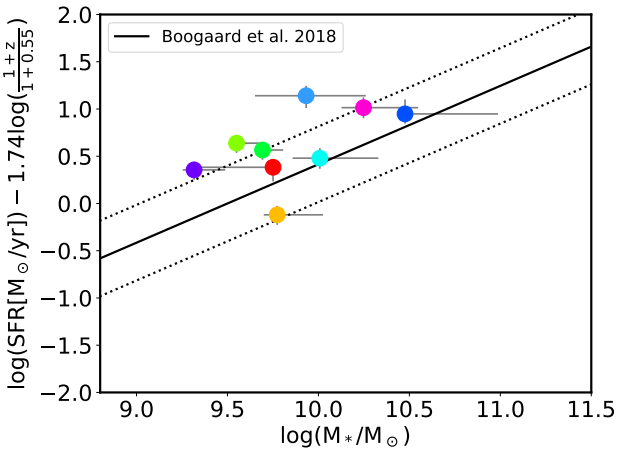

Figure D3. Position of our nine galaxies compared to the main-sequence of star formation (MS). The shown MS (solid line) and its 1σ scatter (dotted lines) is from Boogaard et al. (2018). Redshift evolution of the MS (SFR $\propto (1+z)^{1.74}$) is removed from the plot through the choice of y-axis, which normalises all SFR's to $z = 0.55$.